SURFACE INTEGRAL APPROACHES FOR ELECTROMAGNETIC FIELD PREDICTION

A Project Report

submitted by

D.V.S.S.N.KARTEEKEYA SASTRY

in partial fulfilment of the requirements
for the award of the degree of

BACHELOR OF TECHNOLOGY
&
MASTER OF TECHNOLOGY

DEPARTMENT OF ELECTRICAL ENGINEERING
INDIAN INSTITUTE OF TECHNOLOGY MADRAS.

JUNE 2020

THESIS CERTIFICATE

This is to certify that the thesis titled **SURFACE INTEGRAL APPROACHES FOR ELECTROMAGNETIC FIELD PREDICTION**, submitted by **D.V.S.S.N.KARTEEKEYA SASTRY**, to the Indian Institute of Technology, Madras, for the award of the degree of **Bachelor of Technology and Master of Technology**, is a bona fide record of the research work done by him under our supervision. The contents of this thesis, in full or in parts, have not been submitted to any other Institute or University for the award of any degree or diploma.

Prof. Uday K. Khankhoje
Research Guide
Assistant Professor
Dept. of Electrical Engineering
IIT-Madras, 600 036

Date: 7th June 2020

ACKNOWLEDGEMENTS

First and foremost, I would like to convey my deepest gratitude to my guide, Dr. Uday K. Khankhoje. His guidance over the last three years has not just helped me improve as a researcher but has also had a lasting impact on me. I want to thank Dr. Raffaele Solimene[1] for his valuable suggestions that have immensely improved the quality of this thesis. I also owe my gratitude to Chandan Bhat for his untiring efforts towards this project.

I want to thank my mother for everything she has given me. All that I am, I owe it to her. I am thankful to my sister for being a source of inspiration. Her achievements have set the bar high for me and have motivated me to work harder. I am also very grateful to my father for always believing in me.

I want to thank Sharanya for her unflinching support and love. I am thankful to my friends, Divyashish, Romil, Ram, and Ananya, for their valuable advice and companionship over the last five years. Last but not least, I would like to thank my labmates Ankit, Siddhant, Yaswanth, Yash, Sriram, Aggraj, and Prajosh, for their support and encouragement.

[1] At the Università degli Studi della Campania Luigi Vanvitelli, Aversa, Italy.

ABSTRACT

KEYWORDS: Electromagnetic Scattering, Inverse Problems, Compressive Sensing, Subspace Optimization

This thesis explores the topic of electromagnetic (EM) field prediction in arbitrary scattering scenarios. The method proposed in this thesis does not assume any prior knowledge of the permittivities and the exact geometry of the scatterers. However, the region in between the scatterers is assumed to be homogeneous. A major contribution of this thesis is 'Compressive sensing based subspace optimization method' (CS-SOM). Using CS-SOM, we show that the EM fields in an indoor scattering environment with four scatterers can be reconstructed with an error of 12%, when the number of measurements are 55% of the number of unknowns used to formulate the problem. We also show that the tangential fields on the surfaces of the scatterers can be reconstructed with an error of 22%. We compare CS-SOM to other popular methods in the literature and show that CS-SOM performs better in terms of the error. Finally, we present a few directions in which the current work can be extended. Our approach is a significant departure from traditional ray tracing approaches found in the literature. We use the surface integral formulations which capture wave-matter interactions accurately, use compressive sensing to reduce the number of measurements needed, and finally apply the Huygens' principle to predict the field everywhere.

TABLE OF CONTENTS

LIST OF TABLES

LIST OF FIGURES

ABBREVIATIONS

CS-SOM	Compressive Sensing based Subspace Optimization Method
EM	Electromagnetic
2D	Two dimensional
TM	Transverse Magnetic
EFIE	Electric Field Integral Equation
MFIE	Magnetic Field Integral Equation
SOM	Subspace Optimization Method
SVD	Singular Value Decomposition
CS	Compressive Sensing
RIP	Restrictive Isometry Property
DFT	Discrete Fourier Transform
DCT	Discrete Cosine Transform
FFT	Fast Fourier Transform
NFFT SOM	New FFT Subspace Optimization Method
T-SOM	FFT - Twofold Subspace Optimization Method
IDFT	Inverse Discrete Fourier Transform
AWGN	Additive White Gaussian Noise
SNR	Signal to Noise Ratio
SR	Sampling Rate
3D	Three dimensional
MPME	Maximal Projection on Minimum Eigenspace

CHAPTER 1

INTRODUCTION

This thesis deals with the topic of electromagnetic (EM) field prediction. EM field prediction is crucial to many applications like radar cross-section estimation (Hansen *et al.*, 2006), indoor positioning (Pei *et al.*, 2010; Wu *et al.*, 2015), and Wi-Fi access point planning (Bose and Foh, 2007). Traditional approaches to this problem use the ray tracing technique (Toscano *et al.*, 2003; Degli-Esposti *et al.*, 2004; Ji *et al.*, 2001). However, these techniques have significant drawbacks — they suffer from large errors in near field estimation, are only valid in the high frequency regime, and face difficulties in modelling mutliple scattering events (Remley *et al.*, 2000, Fig. 3). In contrast, the method proposed in this thesis is based on surface integral formulations, and therefore overcomes all the limitations specified above.

Our method relies on a few field measurements to predict the EM field everywhere. It does not assume prior knowledge of the permittivities of the scatterers or their exact geometry. However, the region in between the scatterers is asumed to be homogeneous. The fundamental building blocks of our approach are the Huygens' principle and the Extinction theorem. Using these two theorems and the method of moments (Chew, 1995), we pose a linear inverse problem whose unknowns are the tangential fields on the scatterer surfaces. This linear inverse problem is solved in the framework of the subspace optimization method (Chen, 2009), using a sparsity prior. The estimated tangential fields are then used to predict the fields everywhere.

This thesis only considers two dimensional (2D) geometries that are illuminated by a transverse magnetic (TM) polarization field.

Notation: This thesis uses the following notation: An arrow above a letter ($\vec{\cdot}$) represents a vector quantity. Bold upper case letters (eg. $\boldsymbol{A}$) represent a matrix. Bold lower case letters (eg. $\boldsymbol{a}$, $\boldsymbol{\alpha}$) represent a column vector.

1.1 Outline of the thesis

CHAPTER 2: Some fundamental theorems in EM are introduced. Using these theorems, the problem of predicting the EM fields is posed as a linear inverse problem. This is followed by a brief discussion on the construction of forward solvers.

CHAPTER 3: Solution strategies for the inverse problem are discussed. An important observation in this regard is presented, that the true tangential fields obtained from a forward solver is sparse in a standard basis like the Fourier basis. This observation forms the basis for compressive sensing based subspace optimization method (CS-SOM), an algorithm to solve for the EM fields. Numerical results are presented to quantify the field prediction error. The proposed CS-SOM method is compared with other methods in literature.

CHAPTER 4: A summary of the thesis is presented, along with a detailed discussion on the future directions in which this work may be expanded.

CHAPTER 2

INVERSE PROBLEM FORMULATION

In this section, we present a few theorems that are fundamental to electromagnetics, namely the Huygens' principle, the Extinction theorem, and the Uniqueness theorem. Then we formulate the inverse problem using the aforementioned theorems. Finally, we end the chapter with a brief discussion on the development of the forward solver.

2.1 Preliminaries

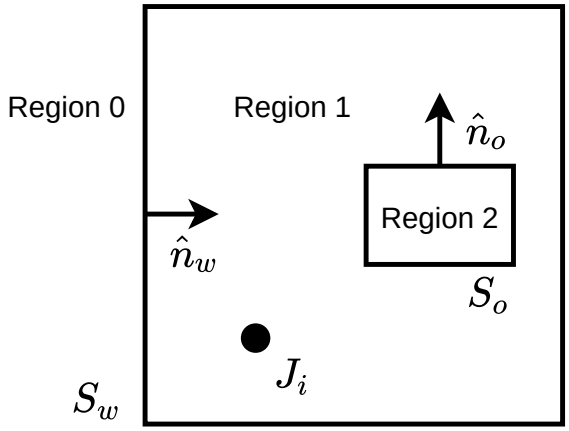

Figure 2.1: The schematic of a 2D inverse scattering problem. J_i is a known source radiating in Region 1 (free space) at a wavelength λ. Region 0 (wall) and Region 2 (object) are scatterers. S_w and S_o are the surfaces of the wall and the object respectively.

The schematic in Fig. 2.1 represents a 2D computational domain which is illuminated by a TM polarization field. Region 1 is considered to be free space $(\epsilon_r = 1, \mu_r = 1)$. In the following Subsection, we derive the Huygens' principle and the Extinction theorem.

2.1.1 The Huygens' principle and the Extinction theorem

The Helmholtz equation in Region 1 is written as (Chew, 1995, Ch. 8.1):

$$\nabla^2\phi(\vec{r}) + k_0^2\phi(\vec{r}) = Q(\vec{r}), \tag{2.1}$$

where $\phi(\vec{r})$ is the (scalar) electric field at the location $\vec{r}$, i.e. $\vec{E}(\vec{r}) = \phi(\vec{r})\hat{z}$; k_0 is the wave number in free space and $Q(\vec{r}) = j\omega\mu_0 J_i(\vec{r})$.

The Green's function in Region 1 is defined as:

$$\nabla^2 g(\vec{r}, \vec{r}') + k_0^2 g(\vec{r}, \vec{r}') = -\delta(\vec{r} - \vec{r}'), \tag{2.2}$$

Multiplying Eq. (2.1) by $g(\vec{r}, \vec{r}')$ and Eq. (2.2) by $\phi(\vec{r})$ and subtracting the two equations, we get:

$$g(\vec{r}, \vec{r}')\nabla^2\phi(\vec{r}) - \phi(\vec{r})\nabla^2 g(\vec{r}, \vec{r}') = g(\vec{r}, \vec{r}')Q(\vec{r}) + \phi(\vec{r})\delta(\vec{r} - \vec{r}') \tag{2.3}$$

Integrating both sides over Region 1 (R_1), we get:

$$\int_{R_1} \Big(g(\vec{r}, \vec{r}')\nabla^2\phi(\vec{r}) - \phi(\vec{r})\nabla^2 g(\vec{r}, \vec{r}')\Big) d^2\vec{r} = \int_{R_1} g(\vec{r}, \vec{r}')Q(\vec{r})d^2\vec{r} + \int_{R_1} \phi(\vec{r})\delta(\vec{r} - \vec{r}')d^2\vec{r} \tag{2.4}$$

We know from vector calculus identities that:

$$\nabla \cdot (g\nabla\phi - \phi\nabla g) = g(\vec{r}, \vec{r}')\nabla^2\phi(\vec{r}) - \phi(\vec{r})\nabla^2 g(\vec{r}, \vec{r}') \tag{2.5}$$

Additionally, the divergence theorem for any vector field $\vec{f}(\vec{r})$ states that:

$$\int_{R_1} \nabla \cdot \vec{f} d^2\vec{r} = \oint_{S_o} \vec{f}.(-\hat{n}_o)dl + \oint_{S_w} \vec{f}.(-\hat{n}_w)dl \tag{2.6}$$

Using Eqs. (2.5) and (2.6), we simplify Eq. (2.4) as:

$$-\oint_{S_o} (g\nabla\phi - \phi\nabla g)\cdot\hat{n}_o dl - \oint_{S_w} (g\nabla\phi - \phi\nabla g)\cdot\hat{n}_w dl = -\phi_i(\vec{r}') + \int_{R_1} \phi(\vec{r})\delta(\vec{r} - \vec{r}')d^2\vec{r}, \tag{2.7}$$

where $\phi_i(\vec{r}') = -\int_{R_1} g(\vec{r}, \vec{r}')Q(\vec{r})d^2\vec{r}$ is the incident field radiated by the source J_i.

Depending on the choice of $\vec{r}'$ in Eq. (2.7), we get two separate, yet important results:

1. In case $\vec{r}' \in R_1$, Eq. (2.7) becomes the Huygens' principle:

$$\phi(\vec{r}') = \phi_i(\vec{r}') - \oint_{S_o} (g(\vec{r},\vec{r}')\nabla\phi_o(\vec{r}) - \phi_o(\vec{r})\nabla g(\vec{r},\vec{r}')) \cdot \hat{n}_o dl - \oint_{S_w} (g(\vec{r},\vec{r}')\nabla\phi_w(\vec{r}) - \phi_w(\vec{r})\nabla g(\vec{r},\vec{r}')) \cdot \hat{n}_w dl, \quad \vec{r}' \in R_1 \quad (2.8)$$

   Eq. (2.8) shows that the total field at any point in Region 1 can be written as a sum of the incident field and the scattered field. The latter is caused by the terms $(\phi_o, \nabla\phi_o \cdot \hat{n}_o)$ and $(\phi_w, \nabla\phi_w \cdot \hat{n})$ on the scatterer surfaces. Detailed analysis of these two terms shows that these are in fact the tangential electric and magnetic fields on the surfaces of the object and the wall respectively. The fact that the scattered field in Region 1 can be determined using the tangential fields on the scatterer surfaces is the essence of the Huygens' principle.

2. When $\vec{r}' \notin R_1$, we get the Extinction theorem:

$$0 = \phi_i(\vec{r}') - \oint_{S_o} (g(\vec{r},\vec{r}')\nabla\phi_o(\vec{r}) - \phi_o(\vec{r})\nabla g(\vec{r},\vec{r}')) \cdot \hat{n}_o dl - \oint_{S_w} (g(\vec{r},\vec{r}')\nabla\phi_w(\vec{r}) - \phi_w(\vec{r})\nabla g(\vec{r},\vec{r}')) \cdot \hat{n}_w dl, \quad \vec{r}' \in R_1 \quad (2.9)$$

   Eq. (2.9) shows that when $\vec{r}' \notin R_1$, the tangential fields on the scatterer surfaces exactly cancel the incident field at that point. Given the source distribution, the Extinction theorem provides a relationship between the tangential electric and the tangential magnetic fields.

2.1.2 The Uniqueness theorem of Electromagnetics

A physical situation always has a unique solution. However, when it is represented in mathematical terms, it may not admit any solution or may admit multiple solutions. This happens due to the over-specification or the under-specification of the boundary conditions. The Uniqueness theorem of EM tells us how to correctly specify the boundary conditions so that the solution is unique.

The Uniqueness theorem states that the EM fields in an environment are uniquely determined once the source and the boundary conditions are specified. The boundary conditions are specified by specifying:

- the tangential electric field on the scatterer surfaces, or
- the tangential magnetic field on the scatterer surfaces, or
- the tangential electric field on a part of the scatterer surface and the tangential magnetic field on the rest of it.

In essence, the Uniqueness theorem implies that the fields can be uniquely determined by specifying either the tangential electric fields or the tangential magnetic fields (in Huygens' principle).

2.2 Outline of the inverse problem

In the previous section, we introduced some theorems that are fundamental to EM. These theorems are also crucial to our understanding of the inverse problem. Therefore, we summarize a few facts about these three theorems below:

FACT 1: The scattered field at any location in Region 1 (in Fig. 2.1) can be found by determining the tangential electric and magnetic fields on the surface of the scatterers (via the Huygens' principle).

FACT 2: It is superfluous to use both the tangential electric and magnetic fields in Eq. (2.8). It is possible to determine the fields uniquely by using any one of the two (via the Uniqueness theorem).

FACT 3: However, since both sets of tangential fields are used, they must be consistent with each other. This consistency is imposed via the relations provided by the Extinction theorem.

Having recapitulated the above facts, we define the inverse problem and provide an outline of our proposed method for solving it. The problem that we address is the following: Consider a room with some objects (such as desks and chairs) in which an active antenna (e.g. a Wi-Fi router) is placed. Can the EM field at each point inside this room be predicted by making a few field measurements? The problem statement is graphically represented by the 2D schematic in Fig. 2.2. An outline of our method is given below:

STEP 1: Measure the field at some random locations in Region 1.

STEP 2: Estimate the tangential fields on the surfaces of the scatterers using the Huygens' principle and the Extinction theorem.

STEP 3: Substitute the estimated tangential fields in the Huygens' principle to predict the field everywhere.

In the rest of the chapter, we flesh out the details of the idea presented above.

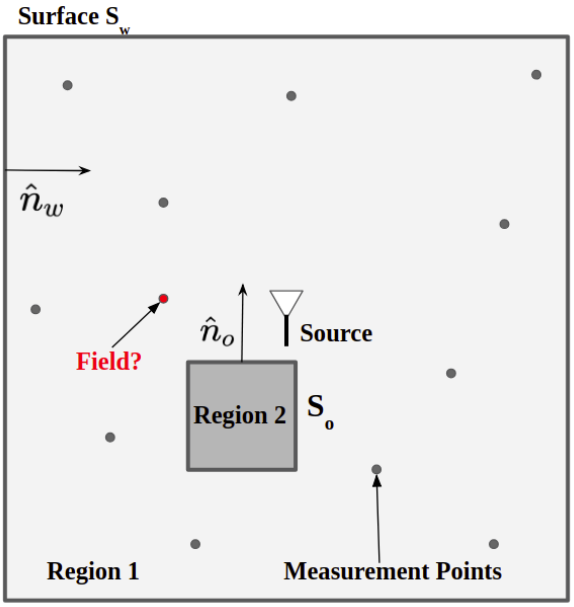

Figure 2.2: Schematic of the problem statement: Can the field be predicted anywhere in Region 1 (a homogeneous medium) by making a few measurements. S_w is the inner surface of the enclosing wall and S_o is the outer surface of the scatterer. $\hat{n}_w$ and $\hat{n}_o$ are normals to the surfaces of the wall and object, respectively.

2.3 Mathematical formulation of the inverse problem

Using Huygens' principle (Balanis, 1999), the z-component of the electric field at any point $\vec{r}$ in Region 1, $\phi(\vec{r})$ can be expressed as:

$$\phi(\vec{r}) = \phi_i(\vec{r}) - \oint_{S_w} [g(\vec{r},\vec{r}')\nabla'\phi_w(\vec{r}') - \phi_w(\vec{r}')\nabla' g(\vec{r},\vec{r}')] \cdot \hat{n}_w \, dl' - \oint_{S_o} [g(\vec{r},\vec{r}')\nabla'\phi_o(\vec{r}') - \phi_o(\vec{r}')\nabla' g(\vec{r},\vec{r}')] \cdot \hat{n}_o \, dl' \quad (2.10)$$

Note that this equation is simply a restatement of Eq. (2.8), with the only difference that $\vec{r}$ and $\vec{r}'$ have been interchanged for notational convenience. $g(\vec{r},\vec{r}') = -(j/4)H_0^{(2)}(k_0|\vec{r}-\vec{r}'|)$ is the free space Green's function in Region 1, $\phi_i(\vec{r})$ is the incident field, ϕ_o, ϕ_w are the tangential electric fields on the object and wall surfaces, and $\hat{n}_w$ and $\hat{n}_o$ are normals to the scattering surfaces of the wall and object, respectively, as shown in Fig. 2.2. It can be shown that $\nabla\phi_o \cdot \hat{n}_o$ and $\nabla\phi_w \cdot \hat{n}_w$ are proportional to the tangential magnetic fields on the object and wall, respectively. S_w is the inner surface of the enclosing wall and S_o is the surface of the scatterer. Note that in Eq. (2.10), $\phi(\vec{r})$ represents the field measurement and is therefore known, whereas the quantities $(\phi_o, \nabla\phi_o.\hat{n}_o)$ and $(\phi_w, \nabla\phi_w.\hat{n}_w)$ are to be estimated, and therefore are the *unknowns*.

We expand the unknowns in known sets of bases $p_n(r)$ and $q_n(r)$ as:

$$\phi_o(r) = \sum_{n=1}^{N_o} a_n^o p_n(r), \qquad \nabla\phi_o(r)\cdot\hat{n}_o = \sum_{n=1}^{N_o} b_n^o p_n(r), \tag{2.11}$$

$$\phi_w(r) = \sum_{n=1}^{N_w} a_n^w q_n(r), \qquad \nabla\phi_w(r)\cdot\hat{n}_w = \sum_{n=1}^{N_w} b_n^w q_n(r), \tag{2.12}$$

where lowercase r denotes the parametrized distance along each surface (S_o or S_w); $p_n(r),\ n = 1, 2, \ldots, N_o$, and $q_n(r), n = 1, 2, \ldots, N_w$ are the sets of basis functions and a_n^o, b_n^o, a_n^w and b_n^w are their respective unknown coefficients.

Substituting Eqs. (2.11) and (2.12) in Eq. (2.10), and considering M locations of field measurement, we get the following linear system of equations:

$$\underbrace{\begin{bmatrix}\boldsymbol{E}\ \boldsymbol{F}\ \boldsymbol{G}\ \boldsymbol{H}\end{bmatrix}}_{\boldsymbol{A}} \underbrace{\begin{bmatrix}\boldsymbol{a}^o\\ \boldsymbol{b}^o\\ \boldsymbol{a}^w\\ \boldsymbol{b}^w\end{bmatrix}}_{\boldsymbol{x}} = \underbrace{\begin{bmatrix}\phi_s(\vec{r}_1)\\ \phi_s(\vec{r}_2)\\ \vdots\\ \phi_s(\vec{r}_M)\end{bmatrix}}_{\boldsymbol{b}} + \boldsymbol{\nu} \tag{2.13}$$

where $\{\boldsymbol{E}, \boldsymbol{F}\} \in \mathbb{C}^{M\times N_o}$, $\{\boldsymbol{G}, \boldsymbol{H}\} \in \mathbb{C}^{M\times N_w}$ compose the system matrix $\boldsymbol{A} \in \mathbb{C}^{M\times N}$, $\boldsymbol{x} \in \mathbb{C}^N$ is a vector with vertically stacked elements $\{\boldsymbol{a}^o, \boldsymbol{b}^o\} \in \mathbb{C}^{N_o}$ and $\{\boldsymbol{a}^w, \boldsymbol{b}^w\} \in \mathbb{C}^{N_w}$, with $N = 2(N_w + N_o)$ being the total number of unknowns. The scattered field at a location $\vec{r}_i$ is $\phi_s(\vec{r}_i)$, which is corrupted by noise given in ν. We call Eq. (2.13) the 'data equation' because it is constructed using the field measurement data.

A standard choice for $p_n(r)$ and $q_n(r)$ is the pulse basis function defined as follows: Let the lengths of the surfaces S_o and S_w be L_o and L_w respectively. Divide the two contours into N_o and N_w segments of equal lengths respectively. With r denoting the parametrized distance along S_o, the pulse basis functions on S_o are defined as:

$$p_n(r) = \begin{cases} 1 & r_{o,n-1} \le r \le r_{o,n} \\ 0 & \text{else} \end{cases} \qquad n \in [1, N_o],\ 0 \le r \le L_o$$

where $r_{o,n}$ denotes the parametrized distance to the end of the i$^{\text{th}}$ segment on S_o. Simi-

larly, with r denoting the parametrized distance along S_w, the pulse basis functions on S_w are defined as:

$$q_n(r) = \begin{cases} 1 & r_{w,n-1} \leq r \leq r_{w,n} \\ 0 & \text{else} \end{cases} \qquad n \in [1, N_w],\ 0 \leq r \leq L_w$$

where $r_{w,n}$ denotes the parametrized distance to the end of the i$^{\text{th}}$ segment on S_w.

The system matrix constructed using the pulse basis is denoted by $\boldsymbol{A}_p = [\boldsymbol{E}_p\, \boldsymbol{F}_p\, \boldsymbol{G}_p\, \boldsymbol{H}_p]$. The elements of each of the submatrices (denoted by their corresponding lower space characters) are given by (Sastry *et al.*, 2019):

$$\begin{aligned} e_{m,k} &= \int_{r_{w,k-1}}^{r_{w,k}} \frac{jk_0}{4\rho_{r_m}} H_1^{(2)}(k_0\rho_m)(\Delta\vec{R}_m \cdot \hat{n})\, dr \\ f_{m,k} &= -\int_{r_{w,k-1}}^{r_{w,k}} \frac{j}{4} H_0^{(2)}(k_0\rho_m)\, dr \\ g_{m,k} &= \int_{r_{o,k-1}}^{r_{o,k}} \frac{jk_0}{4\rho_{r_m}} H_1^{(2)}(k_0\rho_m)(\Delta\vec{R}_m \cdot \hat{n})\, dr \\ h_{m,k} &= -\int_{r_{o,k-1}}^{r_{o,k}} \frac{j}{4} H_0^{(2)}(k_0\rho_m)\, dr \end{aligned} \tag{2.14}$$

where $\Delta\vec{R}_m = \vec{r}_m - \vec{R}(r)$, $\rho_m = |\Delta\vec{R}_m|$ with $\vec{r}_m$ denoting the position vector of the m^{th} measurement point, and $\vec{R}(r)$ denoting the position vector of the point on the respective contour with parametrized distance r.

The data equation was derived using only the Huygens' principle. We have at our disposal one more equation — the Extinction theorem. As stated before, the Extinction theorem relates the tangential electric and magnetic fields. We restate it below:

$$\begin{aligned} 0 = \phi_i(\vec{r}) &- \oint_{S_w} [g(\vec{r},\vec{r}')\nabla'\phi_w(\vec{r}') - \phi_w(\vec{r}')\nabla' g(\vec{r},\vec{r}')] \cdot \hat{n}_w\, dl' \\ &- \oint_{S_o} [g(\vec{r},\vec{r}')\nabla'\phi_o(\vec{r}') - \phi_o(\vec{r}')\nabla' g(\vec{r},\vec{r}')] \cdot \hat{n}_o\, dl' \end{aligned} \tag{2.15}$$

Note that $\vec{r}$ in Eq. (2.15) lies outside Region 1. Substituting Eqs. (2.11) and (2.12) in Eq. (2.15), and setting the basis functions to be the pulse basis functions, we get:

$$\boldsymbol{A}_s\, \boldsymbol{x} = \underbrace{-\left[\phi_{in}(\vec{r}_1^{(s)}) \cdots \phi_{in}(\vec{r}_{\frac{N}{2}}^{(s)})\right]^T}_{\boldsymbol{b}_s}, \tag{2.16}$$

where $\boldsymbol{A}_s \in \mathbb{C}^{\frac{N}{2} \times N}$ is called the the 'state matrix', and $\vec{r}_i^{(s)}$, $i \in [1, \frac{N}{2}]$ are the midpoints of the discretized segments of S_o and S_w (These are $\frac{N}{2}$ in number). We call Eq. (2.16) the 'State Equation' because it gives a relation between the two sets of unknowns.

Evaluating the singular integrals: The 2D Green's function, $g(\vec{r}, \vec{r}') = -(j/4)H_0^{(2)}(k_0|\vec{r} - \vec{r}'|)$ has a singularity when $\vec{r} = \vec{r}'$. In case, any of the integrals involved in our formulation encounter this singularity, they have to be evaluated with sufficient care. The vector $\vec{r}'$ in our formulation always exists on the surfaces S_o and S_w. In the data equation, $\vec{r}$ denotes the measurement locations, which lies in Region 1 by definition. This ensures that $\vec{r}$ is never equal to $\vec{r}'$. Therefore, a singularity is never encountered while populating the data equation. However, in the state equation, the points $\vec{r}_i^{(s)}$ are chosen as the midpoints of the discretized segments of the surfaces. So, whenever the point $\vec{r}_i^{(s)}$ lies on the segment over which the integral is being computed, a singularity is encountered. For each $\vec{r}_i^{(s)}$, there are two singular integrals that are encountered — $\int_{r_{start}}^{r_{end}} g(\vec{r}_i^{(s)}, \vec{r}')dl$ and $\int_{r_{start}}^{r_{end}} \nabla g(\vec{r}_i^{(s)}, \vec{r}') \cdot \hat{n} dl$, where r_{start} and r_{end} are the start and end points respectively of the edge of which $\vec{r}_i^{(s)}$ is the midpoint. It turns out that $\int_{r_{start}}^{r_{end}} g(\vec{r}_i^{(s)}, \vec{r}')dl$ is a convergent integral, and using the small argument approximation for the Hankel's function[1] (Abramowitz and Stegun, 1948), it can be shown that:

$$\int_{r_{start}}^{r_{end}} g(\vec{r}_i^{(s)}, \vec{r}')dl = -\frac{j}{4}h\Big[1 - j\frac{2}{\pi}\Big(\ln\frac{kh}{4} + (\gamma - 1)\Big)\Big],$$

where h is the length of the discretized segment.

However, $\int_{r_{start}}^{r_{end}} \nabla g(\vec{r}_i^{(s)}, \vec{r}') \cdot \hat{n} dl$ is divergent and has to be evaluated carefully (by choosing a suitable integration contour). On doing so, we get $\int_{r_{start}}^{r_{end}} \nabla g(\vec{r}_i^{(s)}, \vec{r}') \cdot \hat{n} dl = -0.5$ (Chew, 1995, Chapter 8.2).

Finally, we refine the outline of our method (mentioned in Section 2.2) using the mathematical framework that we have developed so far.

STEP 1: Measure the field, $\phi(\vec{r}_i)$ at some random locations, $\vec{r}_i = \vec{r}_1, \vec{r}_2, \ldots, \vec{r}_M$ in Region 1. Using the field measurements, populate the vector $\boldsymbol{b}$ in the data equation.

STEP 2: Estimate the tangential fields on the scatterer surfaces by solving the following convex optimization problem:

$$\underset{\boldsymbol{x}}{\text{minimize}} \quad \|\boldsymbol{A}_p\boldsymbol{x} - \boldsymbol{b}\|_2 \leq \epsilon,\ \|\boldsymbol{A}_s\boldsymbol{x} - \boldsymbol{b}_s\|_2 \leq \eta \tag{2.17}$$

[1] $H_0^{(2)}(k\rho) = 1 - j\frac{2}{\pi}(\ln\frac{k\rho}{2} + \gamma)$, where γ is the Euler's constant.

where ϵ is an estimate of the square root of the noise variance, and η is an estimate of the discretization error in the state equation.

STEP 3: Substitute $\boldsymbol{x}$ from above into Eq. (2.10) and calculate the field at S locations. Let the true field at these S locations obtained from the forward solver be $\boldsymbol{f} \in \mathbb{C}^S$ (i.e. this data is generated synthetically). Then we compute the error, $e \in \mathbb{R}$ as

$$e = \|\boldsymbol{B}\boldsymbol{x} - \boldsymbol{f}\|_2 \tag{2.18}$$

where $\boldsymbol{B} \in \mathbb{C}^{S \times N}$ is the matrix obtained from Huygens' principle (2.10) by setting $\vec{r}$ to the locations where the field prediction is desired.

2.4 A note on the forward solver

Before concluding this chapter, we discuss very briefly the construction of the forward solver. For a more rigorous treatment, the reader is directed to (Chew, 1995, Chapter 8). In a forward solver, the information about the source and the permittivities of the scatterers is available, and the tangential fields have to be estimated. A standard method of exactly solving for the tangential fields is to use the Extinction theorem of Region 1 along with the Extinction theorems of the other regions (the scatterers). In order to use the Extinction theorem of the other regions, the Green's function of these regions have to be specified. If these regions are homogeneous with a wave number of k_i, then the Green's function of this region is simply $g_i(\vec{r}, \vec{r}') = -(j/4)H_0^{(2)}(k_i|\vec{r} - \vec{r}'|)$. However, if the scatterers are heterogeneous, the Green's function has to be computed numerically.

Once the Extinction theorems of all the regions are specified, an approach similar to the construction of the state equation is followed, i.e. the tangential fields are expanded in a known basis and the equations are written at the midpoint of each discretized edge. Finally, the tangential fields in different regions are related using boundary conditions. The matrix thus formed is called the 'impedance matrix'. This system is solved for the tangential fields. Once the tangential fields are obtained, as usual, Huygens' principle can be used to calculate the true field everywhere. This class of forward solvers is called the 'Surface Integral Equation' solver it involves integrals that run over the surfaces of the scatterers. Further, since in the beginning of this chapter, we assumed a source with TM polarization ($\vec{E}(\vec{r}) = \phi(\vec{r})\hat{z}$), the surface integral formulation derived is called the 'Electric Field Integral Equation' (EFIE). By duality, one can also derive the 'Magnetic

Field Integral Equation' (MFIE).

The issue of internal resonances: Any discussion on the EFIE is incomplete without a mention of internal resonances. It turns out that when the operating frequency matches the resonant frequency of the cavities formed by the scatterers, the integral operator of the EFIE (or the MFIE) has a non trivial null space (Chew, 1995, Chapter 8.2.3). Equivalently, the impedance matrix formed at these frequencies is ill conditioned (Liu *et al.*, 2004). Therefore, when the EFIE (or the MFIE) is solved at the resonant frequency, the tangential fields obtained are not unique. This problem has been known to the EM community for decades and various approaches have been proposed to overcome this (Glisson *et al.*, 1983; Kajfez *et al.*, 1984; Mongia and Ittipiboon, 1997). One of the popular methods is to use the combined field integral equation, as shown in (Mitzner, 1968).

CHAPTER 3

COMPRESSIVE SENSING BASED SUBSPACE OPTIMIZATION METHOD (CS-SOM)

In this chapter we present compressive sensing subspace optimization method (CS-SOM), an algorithm that is used to solve the optimization problem in Eq. 2.17. We also present the results for a few numerical experiments to demonstrate field prediction. Finally, we compare our method to other popular methods in the literature.

3.1 Mathematical description of CS-SOM

CS-SOM is an algorithm that is an improvisation of the Subspace Optimization Method (SOM) (Chen, 2009). Consider the singular value decomposition (SVD) of the system matrix, $\boldsymbol{A}_p = \sum_i \boldsymbol{u}_i \sigma_i \boldsymbol{v}_i^H$, where $\boldsymbol{u}_i$ and $\boldsymbol{v}_i$ denote the left and right singular vectors of $\boldsymbol{A}_p$ respectively, and σ_i denotes the corresponding singular value (such that $\sigma_i \geq \sigma_{i+1}$). The essential idea of SOM is to recover the unknown signal by projecting it onto two orthogonal subspaces — the 'signal' space, spanned the top L_0 singular vectors of $\boldsymbol{A}_p$, and the 'noise' space, spanned by the remaining $N - L_0$ singular vectors. In the absence of noise, L_0 would simply be the number of independent rows of $\boldsymbol{A}_p$ (typically $\boldsymbol{A}_p$ is underdetermined), and the signal space and noise space would be the row space and the null space of $\boldsymbol{A}_p$. The row space component of the solution can be determined unambiguously, whereas nothing can be said about the null space solution. However, in the presence of noise, the smaller singular values will amplify the noise, and increase the estimation. Therefore, we express the unknown vector as $\boldsymbol{x} = \boldsymbol{x}_s + \boldsymbol{x}_n$, where $\boldsymbol{x}_s$ and $\boldsymbol{x}_n$ correspond to the signal space and noise space components respectively, and determine them as follows:

Signal space estimation: The signal space component, $\boldsymbol{x}_s$ is determined using a L_0 term truncated SVD solution of the data equation:

$$\boldsymbol{x}_s = \sum_{i=1}^{L_o} \left(\frac{\boldsymbol{u}_i^H \boldsymbol{b}}{\sigma_i} \right) \boldsymbol{v}_i, \tag{3.1}$$

where L_0 is chosen using the Morozov discrepancy principle (Morozov and Grebennikov, 2005), i.e. L_o is the smallest number such that $\|\boldsymbol{A}_p\boldsymbol{x}_s - b\|_2 < \epsilon$, where ϵ is the square root of the noise variance, which in many situations, is reasonably known. The problem is not very sensitive to the exact choice of L_o, as the remaining components are determined in the next stage; various studies have also corroborated this observation (Chen, 2009; Sanghvi *et al.*, 2019).

(ii) **Noise space estimation:** In general, the noise space component, $\boldsymbol{x}_n$ cannot be recovered. However, when there is some prior knowledge about the quantity to be recovered, this information can be leveraged to recover $\boldsymbol{x}_n$ to a certain extent. In our case, the prior information comes from a crucial observation regarding the true tangential fields. For the scenario in Fig. 2.2, when the true tangential fields are computed using a forward solver, and the DFT of these tangential fields is plotted (see Fig. 3.1), we observe that most of the coefficients have a very low magnitude, i.e. the unknown quantity exhibits sparsity in DFT basis.

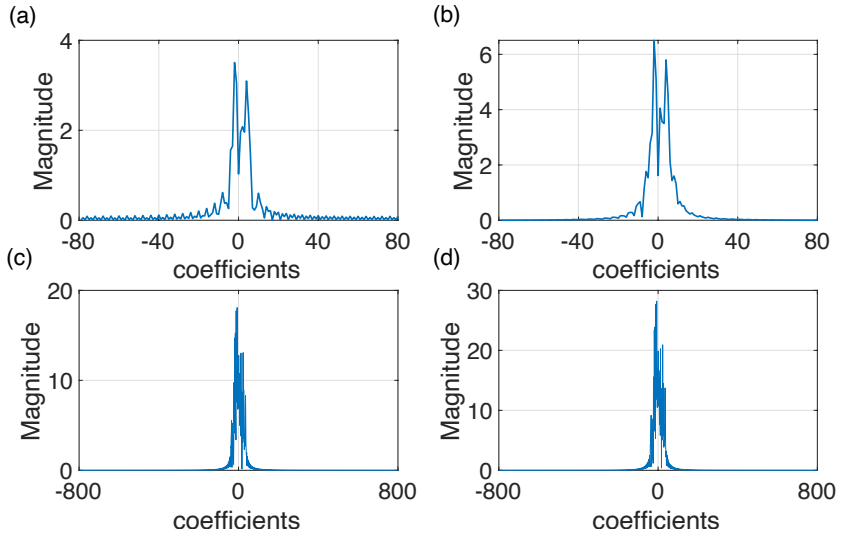

Figure 3.1: DFT coefficients of the tangential fields (a) $\nabla\phi_o \cdot \hat{n}_o$, (b) ϕ_o on the scattering surface S_o and (c) $\nabla\phi_w \cdot \hat{n}_w$, (d) ϕ_w on the scattering surface S_w as shown in Fig. 2.2. Most coefficients have very low magnitudes.

This observation can be exploited to reconstruct the EM fields, by leveraging ideas of Compressive sensing (CS) (Candes *et al.*, 2008). CS principles state that a sparse signal can be recovered from undersampled linear measurements, provided the observation matrix satisfies the Restrictive isometry property (RIP). The RIP, however, is in general difficult to verify for deterministic matrices. So, we apply CS principles heuristically, an approach that has gained popularity in the EM community (Massa *et al.*, 2015). Thus, keeping $\boldsymbol{x}_s$ constant (at the value obtained from Eq. (3.1)), we propose to

solve for $\boldsymbol{x}_n$ using the following convex optimization problem:

$$\begin{aligned} \underset{\boldsymbol{x}_n}{\text{minimize}} \quad & \|\boldsymbol{M}(\boldsymbol{x}_s + \boldsymbol{x}_n)\|_1 \\ \text{subject to} \quad & \|\boldsymbol{A}_p\boldsymbol{x}_n - (\boldsymbol{b} - \boldsymbol{A}_p\boldsymbol{x}_s)\|_2 \leq \epsilon, \\ & \|\boldsymbol{A}_s\boldsymbol{x}_n - (\boldsymbol{b}_s - \boldsymbol{A}_s\boldsymbol{x}_s)\|_2 \leq \eta \end{aligned} \tag{3.2}$$

where $\boldsymbol{M} = \boldsymbol{\mathcal{F}}, \boldsymbol{\mathcal{W}}$, or $\boldsymbol{\mathcal{D}}$ are the DFT, wavelet or DCT bases, respectively, chosen as candidates for sparse representations. As before, ϵ is an estimate of the square root of the noise variance, and η is an estimate of the discretization error in the state equation.

A note on sparsity in EM reconstruction problems: A natural question arises regarding the applicability of sparse recovery in general EM problems. As it turns out, sparsity is indeed a general principle in EM problems involving radiation-like operators. It is shown in (Chen, 2018, Fig. 6.14) that the right singular vectors corresponding to the highest singular values of the state operator resemble low-frequency Fourier bases, whereas those corresponding to the lower singular values resemble high-frequency bases. Therefore, it is clear that the solution is dominated by the highest singular values, and thus the low-frequency Fourier bases. Hence, the idea of sparse reconstruction can be used as a general principle in all EM problems involving radiation-like operators.

3.2 Numerical results

In this section we demonstrate the process of field prediction using our method. We describe the simulation setup, define the error metrics, and present the results for various scenarios.

3.2.1 Simulation Setup

The simulation domain is a square region of $10\lambda \times 10\lambda$ with four objects inside. All four objects have different permittivities and are within an outer wall, which is assumed to be infinitely thick (a realistic assumption because it is lossy). The simulation setup is shown in Fig. 3.2. Objects 1,2,3 and 4 are centered at $(-2.5\lambda, 1.5\lambda)$, $(2\lambda, 2\lambda)$,

$(1\lambda, -2.5\lambda)$ and $(-2.5\lambda, -1\lambda)$ respectively, where λ is the wavelength; The relative permittivities of the objects 1, 2, 3, 4 and the wall are $\epsilon_{r1} = 3.7 - 2.1j$, $\epsilon_{r2} = 1.7 - 1.1j$, $\epsilon_{r3} = 2.7 - 3.7j$, $\epsilon_{r4} = 1.2 - 1.1j$ and $\epsilon_{rw} = 3.7 - 2.1j$ respectively (lossy, so as to mimic real life materials such as a concrete wall, etc.). Object 1 is a square of side λ, object 2 is a cirle with radius 0.75λ, object 3 is a rectangle with dimensions $1\lambda \times 2.5\lambda$ and object 4 is a circle with radius 1λ. The source is at $\vec{r_0} = (0.5\lambda, -0.75\lambda)$, and it radiates a cylindrical plane wave of the form: $\phi_i(\vec{r}) = H_0^{(2)}(k_0|\vec{r} - \vec{r_0}|)$. Note that the permittivity and the true geometry of the objects are used only in the forward solver to generate the synthetic measurements.

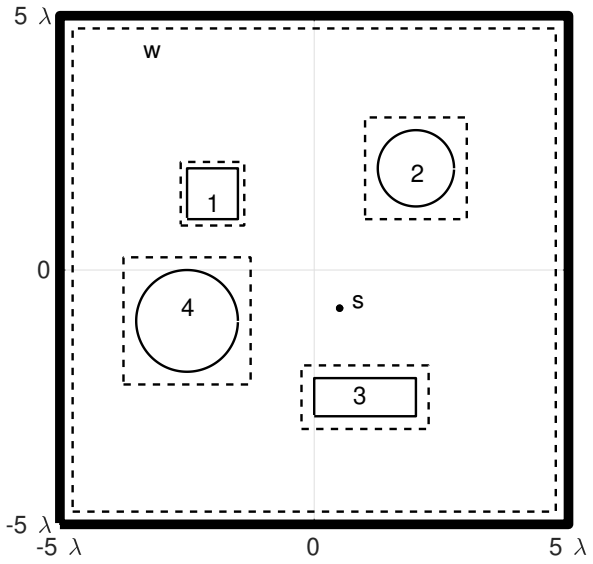

Figure 3.2: The schematic of the simulation domain of dimension $10\lambda \times 10\lambda$. The domain includes an outer wall, 4 objects and a source. The objects 1,2,3 and 4 are centered at $(-2.5\lambda, 1.5\lambda)$, $(2\lambda, 2\lambda)$, $(1\lambda, -2.5\lambda)$ and $(-2.5\lambda, -1\lambda)$ respectively. The source is placed at $(0.5\lambda, -0.75\lambda)$ and 'w' is the outer boundary. The dotted contours represent approximate geometry of the objects used in the field reconstruction algorithm.

3.2.2 Generating the 'True' fields

The true tangential fields are obtained using the Surface Integral Equation (SIE) method, using pulse basis to expand the tangential fields on the surfaces of the scatterers. The procedure for construction a SIE solver is given in Section 2.4. A spatial discretization of $\lambda/40$ (of the surfaces of the scatterers) is considered to ensure numerical convergence. The true field at all points is obtained by substituting the true tangential fields in Huygens' principle (Eq. (2.10)). To verify the correctness of our forward solver,

we simulate the scattering from a single infinite cylinder of radius λ and validated it with the Mie series solution. We present the details of this comparison below. Fig. 3.3 shows the scattered field from a single infinite cylinder computed using the Mie series solution and our surface integral solver. The radius of the cylinder is 1m and it's relative permittivity is $\epsilon_r = 2$. The scattered field is computed on a circular contour of radius 2m. The incident wave is a 2D plane wave of wavelength $\lambda = 1$m. When the surface of the cylinder is discretized at $\lambda/40$, the relative error between the two solutions is 1.4%. We also present a study of the error with different discretization in Table 3.1. It can be seen that as the discretization is increased, the error decreases monotonically.

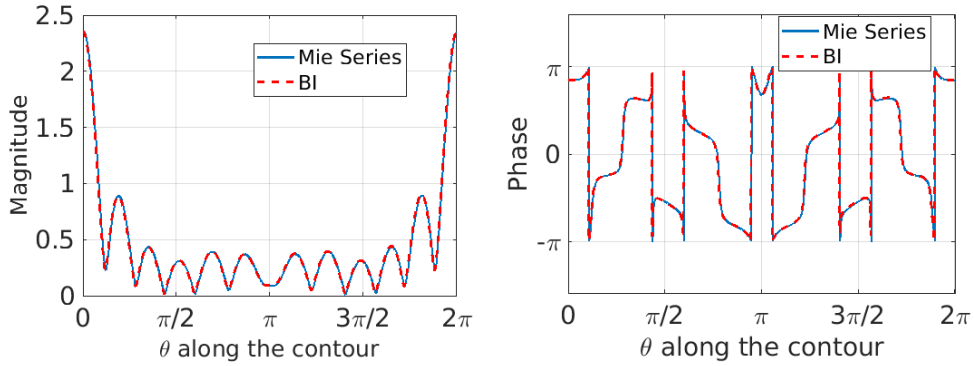

(a) Magnitude (b) Phase

Figure 3.3: Comparison of the forward solver with the Mie series solution. The figure shows the scattered field by a single infinite cylinder of radius 1m with a relative permittivity of $\epsilon_r = 2$. The incident wave is a plane wave. For BI we choose a discretization of $\lambda/40$ which gives an error of 1.4%. The scattered field is calculated along a contour of radius 2m from the center of the cylinder.

Discretization	$\lambda/10$	$\lambda/15$	$\lambda/20$	$\lambda/25$	$\lambda/30$	$\lambda/35$	$\lambda/40$	$\lambda/50$
Error %	10.8	5.9	4.42	3.4	2.9	2.3	1.4	1.3

Table 3.1: The table shows the error between the scattered field from a single infinite cylinder calculated using the Mie series solution and the forward solver for various discretizations. The discretization is increased from $\lambda/10$ to $\lambda/50$ and the error is calculated in the scattered field.

As noted at the end of Section 2.4, the EFIE is known to display numerical issues related to cavity resonances. It turns out that our formulation and the choice of frequency is not affected by the issue of cavity resonances as detailed below. In order to demonstrate this, we plot the reciprocal of the condition number of the impedance matrix (system matrix of the forward solver) in a range of frequencies around the frequency chosen in our paper. It is known that internal resonances can be inferred from

the condition number (Liu *et al.*, 2004), since at resonance the lowest singular value tends to zero, and therefore the reciprocal of the condition number also tends to zero. Fig. 3.4 shows the variation of the inverse of condition number with the frequency of operation, thus reassuring us that our formulation is not affected by this issue in the neighbourhood of this frequency.

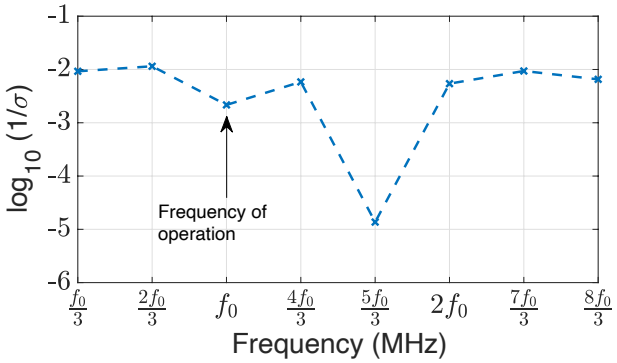

Figure 3.4: Plot of the $\log(1/\sigma)$, where σ is the condition number of the impedance matrix at a particular frequency in a frequency range between $\frac{f_0}{3}$ and $\frac{8f_0}{3}$. $f_0 = 15$MHz is the operating frequency.

The measurements for the inverse solver are generated synthetically, using the true tangential fields from the forward solver. The measurements are then corrupted with additive white Gaussian noise (AWGN) with a signal to noise ratio (SNR) of 25 dB and 10 dB.

3.2.3 Numerical considerations in the inverse problem

In order to demonstrate that the inverse solver requires only the approximate location and geometry of the scatterers, while predicting the field we don't assume the knowledge of the exact shape of the scatterer. Instead, as shown in Fig. 3.2 by means of dotted contours around the objects, we approximate the geometry of the object by a bounding box that encloses the object. The data equation and the state equation are obtained using a uniform discretization of $\lambda/5$ along the dotted contours. This is based on our numerical experiments which showed that a discretization of $\lambda/5$ gives the optimal trade-off between accuracy and computational cost. In general, the number of unknowns for the tangential fields varies with the number of objects and the problem discretization. At a discretization of $\lambda/5$, the total number of unknowns as 704. In the second stage of CS-SOM (see Eq. (3.2)), we note that the value of η is chosen to be the discretization

error in the state equation. This is found by computing the 'state residual' defined as, $\|\boldsymbol{A}_s\boldsymbol{x}_{true} - \boldsymbol{b}_s\|/\|\boldsymbol{b}_s\|$, where $\boldsymbol{x}_{true}$ denotes the true tangential fields calculated using the forward solver. At a discretization of $\lambda/5$, we obtain a state residual of around 0.06. Therefore, in all our experiments we set $\eta = 0.1$.

For ease of notation, we define sampling rate (SR) as the ratio of number of measurements to the number of unknowns. We perform numerical experiments for three values of SR : 0.3 (212 measurements), 0.55 (387 measurements) and 0.8 (563 measurements).

Applicability of compressive sensing when $M > \frac{N}{2}$: In the cases where the number of measurements M exceeds the $\frac{N}{2}$, a natural question arises regarding whether or not there are more equations than the number of variables. To recap: the estimation matrix, $\boldsymbol{A}_p$, is of size $M \times N$, whereas the system matrix, $\boldsymbol{A}_s$, is of size $\frac{N}{2} \times N$, where M, N refer to the number of measurements and variables, respectively. Thus, when SR > 0.5, i.e. $M > \frac{N}{2}$, the total number of equations exceed N. To investigate this further, we construct a "composite" system matrix such that $\tilde{\boldsymbol{A}} = \begin{pmatrix} \boldsymbol{A}_p \\ \boldsymbol{A}_s \end{pmatrix}$, and then study its singular value spectrum in Fig. 3.5 for varying values of SR. Evidently:
(i) Even by the conservative definition of rank, which includes very small but non-zero singular values, the rank of the composite system does not exceed N.
(ii) If we take a more realistic scenario and consider singular values within a factor of 10^6 of the maximum singular value, the number of significant singular values is well below N.

Therefore, even though the composite matrix $\tilde{\boldsymbol{A}}$ is overdetermined, it does not have full column rank. Thus, the use of a priori information towards compressive sensing solutions remains legitimate.

3.2.4 Error Metric Definition

We define two error metrics — the tangential field error, (Δ_T), and the error in reconstruction on the 2D grid (Δ_G). The tangential field error is defined as,

$$\Delta_T = \frac{\|\boldsymbol{x}_{est} - \boldsymbol{x}_{true}\|_2}{\|\boldsymbol{x}_{true}\|_2} \tag{3.3}$$

where $\boldsymbol{x}_{est}$ and $\boldsymbol{x}_{true}$ are the estimated and true tangential fields respectively.

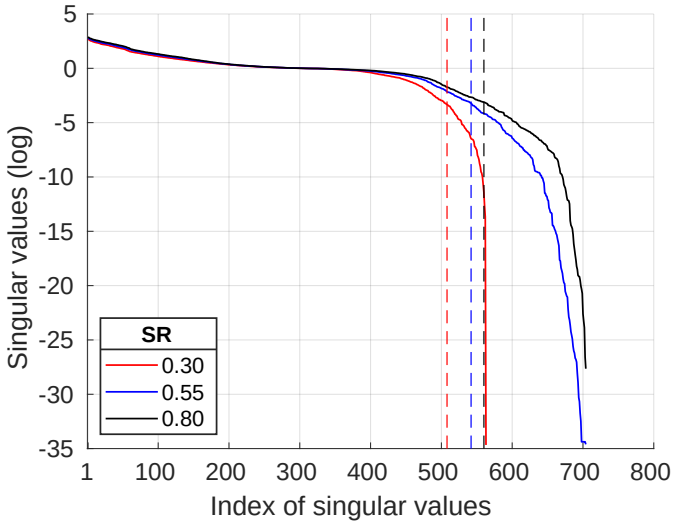

Figure 3.5: Study of the singular values of the composite system matrix $\tilde{\boldsymbol{A}}$ as a function of sampling rate. The dashed lines for each color indicate the singular value index where the singular values goes below a factor of 10^6 from the maximum singular value.

The field is estimated over the $10\lambda \times 10\lambda$ region, discretized on a grid of discretization $\lambda/20$. The error in reconstruction on the 2D grid is calculated as:

$$\text{error } (\Delta_G) = \frac{\|\boldsymbol{\phi}_{est} - \boldsymbol{\phi}_{true}\|_2}{\|\boldsymbol{\phi}_{true}\|_2} \tag{3.4}$$

where $\boldsymbol{\phi}_{est}$ and $\boldsymbol{\phi}_{true}$ are the estimated and true fields over the 2D grid of points respectively.

We also define the relative error at a location $\vec{r}$ as:

$$\frac{|\phi_{est}(\vec{r}) - \phi_{true}(\vec{r})|}{|\phi_{true}(\vec{r})|} \tag{3.5}$$

where $\phi_{est}(\vec{r})$ and $\phi_{true}(\vec{r})$ are the estimated and true fields at $\vec{r}$ respectively.

The locations inside the object and those that are very close to the scatterer surfaces (at a distance less than $\lambda/10$ from the approximate surfaces of the objects) are not considered in the error calculation.

3.2.5 Field prediction using random measurements

All the figures presented in the Section are for an SR of 0.55 (387 measurements) and for an SNR of 25dB. The measurement locations are chosen randomly in the region in

between the scatterers. The reconstruction of the tangential fields for an SR 0f 0.55 and 25dB SNR can be visually appreciated in Figs. 3.6. The average error in the reconstructed tangential fields (Δ_T) for this case over 100 monte carlo iterations is 22%.

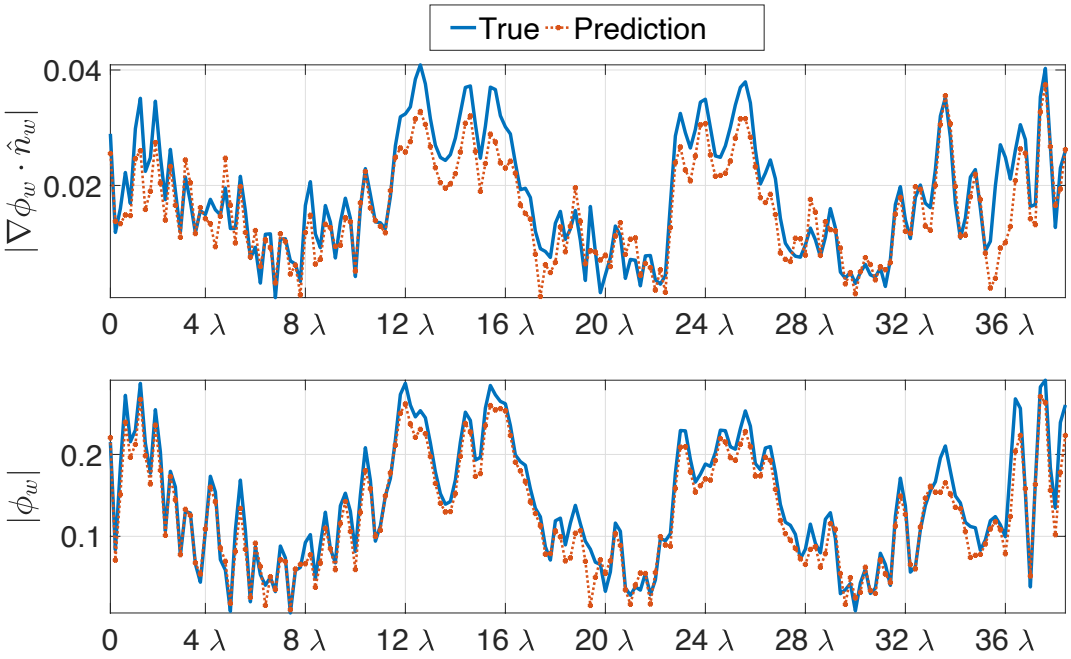

Figure 3.6: Comparison of the magnitudes of the estimated and true tangential fields on the surface of the inexact wall, obtained for 387 measurements (0.55 times the number of unknowns). The measurements are noise corrupted by 25 dB SNR.

We calculate the field over a circular contour of radius 4.2λ, centered at the origin using the true tangential fields and the recovered tangential fields, and plot them in Fig. 3.7. It can be seen that the predicted fields match the true fields.

Next, we predict the fields on a 2D grid in the computational domain with a pitch of $\lambda/20$. The magnitude and phase of the true and predicted fields over the 2D grid are given in Figs. 3.8 and 3.9. The average reconstruction error on the grid (Δ_G) over 100 monte carlo iterations for and SR of 0.55 and 25dB SNR is 12%.

Then we plot the relative error at each prediction location in Fig. 3.10 along with a histogram of the relative errors calculated at each of the locations. It can be seen that the error at over 80% locations is less than 10%. In fact, we can also conclude that the error is highest in the region in between the objects that are close and near the boundary of the wall.

We tabulate Δ_G and Δ_T for different SRs and SNRs of 10dB and 25dB in Table 3.2.

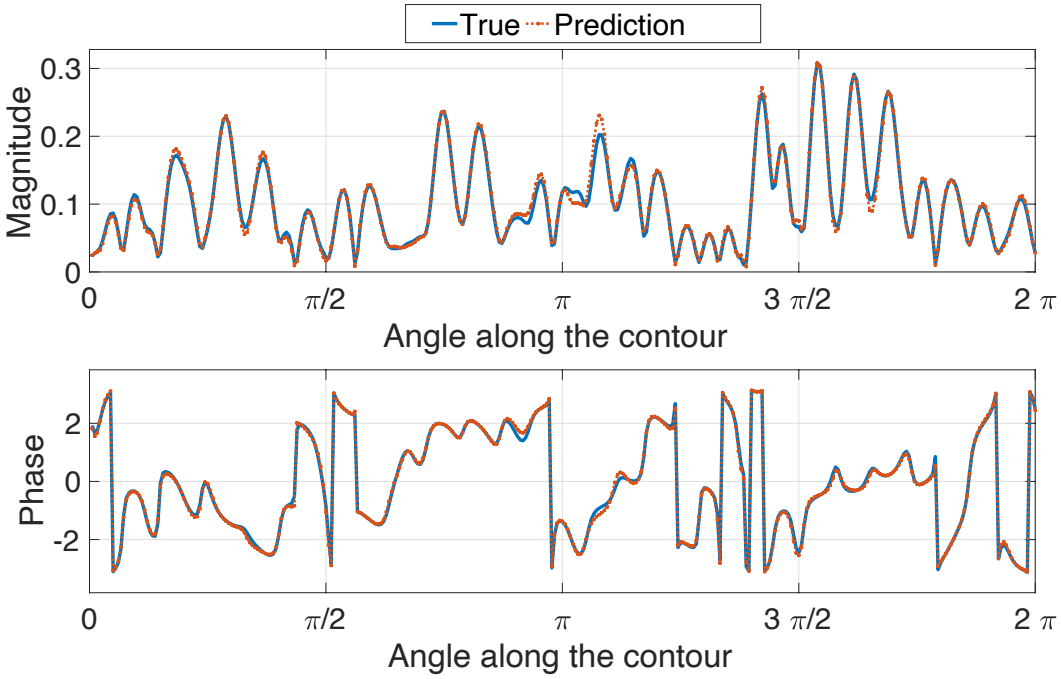

Figure 3.7: Comparison of reconstructed and true fields (magnitude and phase) over a contour of radius 4.2 λ obtained for 0.55x sampling rate (387 measurements). The measurements are noise corrupted by 25 dB SNR.

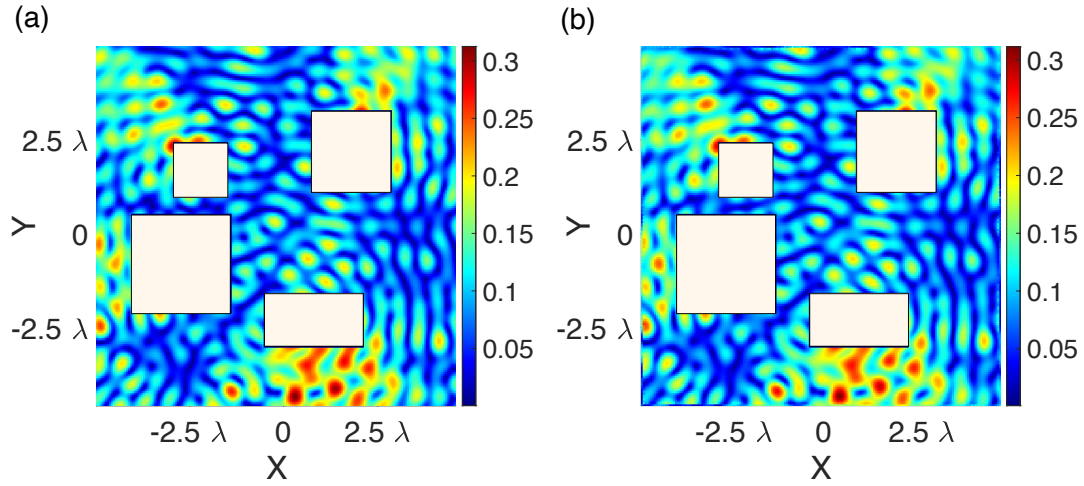

Figure 3.8: The magnitude of (a) true and (b) reconstructed 2D fields over a $10\lambda \times 10\lambda$ grid, obtained for 0.55x sampling rate (387 measurements). The measurements are noise corrupted by 25 dB SNR. The colorbar shows the field magnitude in V/m.

As expected, the error reduces as the number of measurements increases. However this improvement reduces as we go to higher SRs. This can be explained using the SVD of the system matrices (see Fig. 3.5).

In order to study the variation of the results with geometry, we also perform experiments with different number of objects (two to four). The errors for these experiments

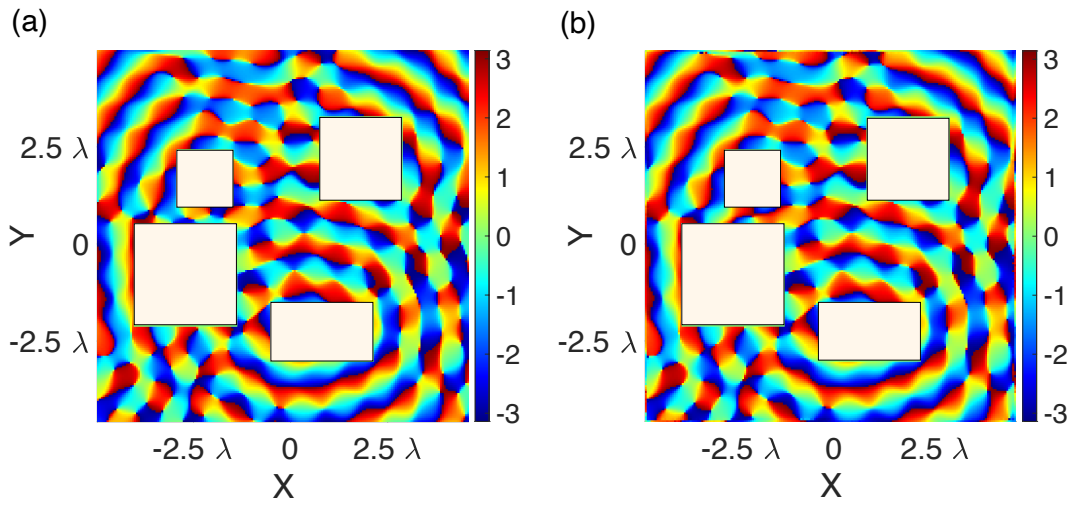

Figure 3.9: The phase of (a) true and (b) reconstructed 2D fields over a $10\lambda \times 10\lambda$ grid, obtained for 0.55x sampling rate (387 measurements). The measurements are noise corrupted by 25 dB SNR. The colorbar shows the phase in radians.

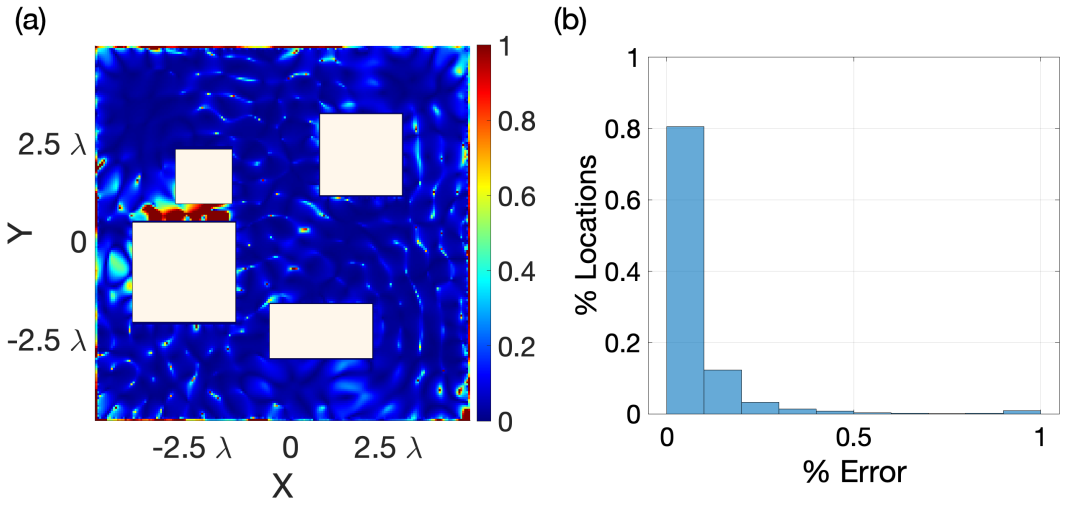

Figure 3.10: (a) Relative error (see (3.5)) in the prediction of total field over a $10\lambda \times 10\lambda$ grid discretized at $\lambda/20$. The prediction is obtained for 0.55x sampling rate (387 measurements) . The measurements are noise corrupted by 25 dB SNR, and (b) Histogram of normalized error over different locations of the simulation domain in Fig. 3.10 (a). 80 % of the locations, have less than 10 % prediction error with an average error of 12 %

are presented in Table 3.3. It can be seen that the variation in the error is within the standard deviation. Therefore, we conclude that as the complexity of the scattering environment increases, the reconstruction error does not change significantly.

SNR (dB)		Measurements/Sampling Rate					
		212/ 0.3x		387/0.55x		563/0.8x	
		Δ_G	Δ_T	Δ_G	Δ_T	Δ_G	Δ_T
25	Mean	23	32	12	22	8	19
	Max	32	43	17	29	11	24
	Min	15	24	7	17	5	16
	SD	3	3	2	3	1	2
10	Mean	45	45	31	36	24	30
	Max	54	53	37	41	28	39
	Min	39	39	25	30	20	24
	SD	3	3	2	3	2	3

Table 3.2: Percentage error in the predicted field (Δ_G) and recovered tangential field (Δ_T) for different measurement modalities (different number of measurements and SNR values) over a $10\lambda \times 10\lambda$ grid calculated for 100 monte carlo trials. SD is the standard deviation.

SNR (dB)		Number of Objects					
		2		3		4	
		Δ_G	Δ_T	Δ_G	Δ_T	Δ_G	Δ_T
25	Mean	10	17	9	17	12	22
	Max	19	13	14	22	17	29
	Min	6	25	6	14	7	11
	SD	3	3	2	2	2	3
10	Mean	30	31	30	32	31	36
	Max	37	38	39	46	37	47
	Min	24	25	27	28	25	30
	SD	3	3	2	4	2	3

Table 3.3: Percentage error in the predicted field (Δ_G) and recovered tangential field (Δ_T) for different number of objects over a $10\lambda \times 10\lambda$ grid, for 0.55x sampling rate. The error was calculated for 100 monte carlo trials. SD is the standard deviation. The number objects are considered in serial wise as shown in Fig 3.2.

3.3 Comparison with related schemes

In this section, we present a comparison of CS-SOM with other popular methods in the literature.

3.3.1 Truncated SVD

The truncated SVD solution (of the composite matrix $\tilde{\boldsymbol{A}} = \begin{pmatrix} \boldsymbol{A}_p \\ \boldsymbol{A}_s \end{pmatrix}$) is the most natural choice when solving a linear system with noisy data. Since the state equation is not corrupted by noise, we determine the truncation limit using only the data equation's

residual, i.e. we retain the minimum number of singular values so as to satisfy $\|\boldsymbol{A}_p\boldsymbol{x} - \boldsymbol{b}\| < \epsilon$, where ϵ is an estimate of the square root of the noise variance. Since this approach does not exploit any prior knowledge about the problem, it performs poorly (in comparison to CS-SOM). For an SR of 0.55 and 25dB SNR, over 100 monte carlo trials, we obtain $\Delta_G = 19\%$ and $\Delta_T = 30\%$.

3.3.2 Vanilla CS

We can also use CS directly to the problem without the SOM framework. This is achieved by:

$$\begin{aligned} \underset{\boldsymbol{\xi}}{\text{minimize}} \quad & \|\boldsymbol{\xi}\|_1 \\ \text{subject to} \quad & \|\boldsymbol{A}_p\boldsymbol{K}\boldsymbol{\xi} - \boldsymbol{b}\|_2 \leq \epsilon, \\ & \|\boldsymbol{A}_s\boldsymbol{K}\boldsymbol{\xi} - \boldsymbol{b}_s\|_2 \leq \eta \end{aligned} \tag{3.6}$$

where $\boldsymbol{K}$ is a linear transformation with coefficients $\boldsymbol{\xi}$. This approach also leads to a higher error than CS-SOM. It achieves an average of $\Delta_G = 14\%$ and $\Delta_T = 25\%$ in the case of a sampling rate of 0.55 and 25 dB SNR. Our proposed CS-SOM approach can be thought of as a synthesis of these two approaches, and thus gives superior results.

3.3.3 Low pass filtering approaches

In CS-SOM, we recover the noise space component by penalizing the l_1 norm of the solution in a standard basis. Another popular way of exploiting sparsity is to regularize the solution by only choosing the low frequency basis coefficients. There are two popular methods, also based on SOM, that follow this approach, namely the New FFT SOM (NFFT SOM) (Wei *et al.*, 2016) and FFT - Twofold SOM (T-SOM) (Chen, 2018).

In NFFT SOM, the signal is decomposed as $\boldsymbol{x} = \boldsymbol{x}_s + \boldsymbol{F}\boldsymbol{\alpha}$, where $\boldsymbol{F}$ is a *complete* Fourier basis. In the first stage of the method, $\boldsymbol{x}_s$ is recovered using Morozov's principle — using the first L right singular vectors of the system matrix $\boldsymbol{A}_p$. This is identical to the first stage of CS-SOM. The second stage of NFFT SOM is implemented via a

constrained optimization approach as follows:

$$\underset{\alpha}{\text{minimize}} \quad \|\boldsymbol{F}\boldsymbol{\alpha}\|_2 \tag{3.7}$$

$$\text{subject to:} \quad \|\boldsymbol{A}_s(\boldsymbol{x}_s + \boldsymbol{F}\boldsymbol{\alpha}) - \boldsymbol{b}_s\|_2 \leq \eta, \tag{3.8}$$

$$\|\boldsymbol{A}_p(\boldsymbol{x}_s + \boldsymbol{F}\boldsymbol{\alpha}) - \boldsymbol{b}\|_2 \leq \epsilon, \tag{3.9}$$

where ϵ is an estimate of the square root of the noise variance, and η is an estimate of the discretization error in the state equation..

In T-SOM, the unknown signal is decomposed as $\boldsymbol{x} = \boldsymbol{x}_s + \boldsymbol{V}_n\boldsymbol{V}_n^H\bar{\boldsymbol{F}}\boldsymbol{\beta}$, where $\bar{\boldsymbol{F}}$ is inverse Discrete Fourier Transform matrix (IDFT) and $\boldsymbol{V}_n$ is the minor part of the right singular vectors of the system matrix $\boldsymbol{A}_p$. The first stage of this method is identical to that of CS-SOM i.e., $\boldsymbol{x}_s$ is recovered using the first L right singular vectors of the system matrix $\boldsymbol{A}_p$. The second stage of T-SOM is implemented via a constrained optimization approach as follows:

$$\underset{\beta}{\text{minimize}} \quad \|\boldsymbol{D}\bar{\boldsymbol{F}}\boldsymbol{\beta}\|_2 \tag{3.10}$$

$$\text{subject to:} \quad \|\boldsymbol{A}_s(\boldsymbol{x}_s + \boldsymbol{D}\bar{\boldsymbol{F}}\boldsymbol{\beta}) - \boldsymbol{b}_s\|_2 \leq \eta, \tag{3.11}$$

$$\|\boldsymbol{A}_p(\boldsymbol{x}_s + \boldsymbol{D}\bar{\boldsymbol{F}}\boldsymbol{\beta}) - \boldsymbol{b}\|_2 \leq \epsilon, \tag{3.12}$$

where $\bar{\boldsymbol{F}}\boldsymbol{\beta} = [\bar{\boldsymbol{F}}_1, \bar{\boldsymbol{F}}_2 \cdots \bar{\boldsymbol{F}}_{M_0}]\boldsymbol{\beta}$ and $M_0 (< N)$ is the number of coefficients. $\boldsymbol{D} = \boldsymbol{V}_n\boldsymbol{V}_n^H = \boldsymbol{I} - \boldsymbol{V}_s\boldsymbol{V}_s^H$, $\boldsymbol{V}_s$ is the major part of the right singular vectors of the system matrix $\boldsymbol{A}_p$. As before, ϵ is an estimate of the square root of the noise variance, and η is an estimate of the discretization error in the state equation.

We find that our method outperforms both these methods. This is quantified in Table 3.4 for a sampling rate of 0.55 and an SNR of 25dB. We do note, however, that CS-SOM has a higher computational run time than NFFT SOM or T-SOM.

Method $\rightarrow$ $\downarrow$ Error type	CS-SOM	NFFT SOM	T-SOM		
			$M_0/N = 0.3$	$M_0/N = 0.5$	$M_0/N = 0.7$
Δ_G	12	15	16	15	15
Δ_T	22	30	32	29	31

Table 3.4: Comparison of error for different methods at a sampling rate of 0.55 and an SNR of 25dB.

CHAPTER 4

CONCLUSION

In this chapter, we present a discussion of the future directions in which this work can be extended. Then, we conclude this thesis with a short summary of the results presented.

4.1 Future extensions

Since the approach presented in this thesis differs significantly from ray tracing approaches in literature, it has various applications, and can be extended in multiple exciting directions. We present a few of these below.

4.1.1 Sensor Placement

In this thesis, we consider the measurement locations to be random. A realization of 50 random samples (for a geometry with one object and a surrounding wall) is shown in Fig. 4.1. It can be seen that random samples are closely spaced and tend to form clusters. This increases the redundancy in the system, thus increasing the number of measurements without decreasing the reconstruction error significantly. From a linear algebra perspective, closely spaced samples correspond to linearly dependent rows in the system matrix which leads to deterioration in error performance. Therefore, random sampling is not the optimal way of selecting samples.

The problem of finding the optimal sampling locations is called 'sensor placement' in the literature. Formally, sensor placement is the selection of the 'best' M sensor locations out of N_0 ($N_0 \gg M$) possible locations in the presence of noise. When the measurements and the unknown have a linear relationship, it can be equivalently defined as the selection of those M rows out of N_0 rows in the system matrix, which contains the *most* information.

The most obvious way to solve the problem of sensor placement is to try out all the $\binom{N_0}{M}$ possibilities and to choose that combination which results in the least error.

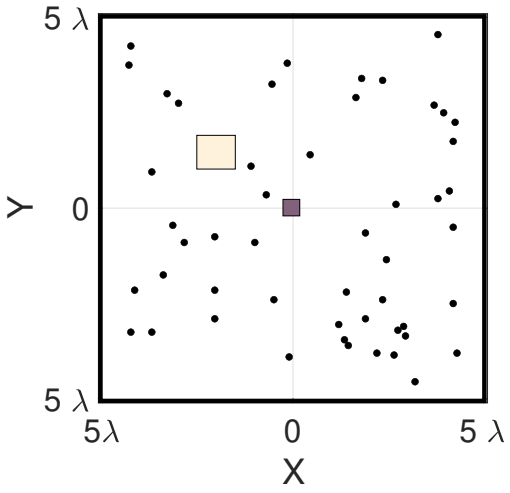

Figure 4.1: A realization of 50 random samples in a room with a single scattering object is shown. It can seen that the samples are not uniformly spaced and tend to form clusters.

This combinatorial approach is NP-hard and is intractable even for small values of N (eg. $\binom{50}{25} > 10^{14}$). The problem of obtaining the optimal sensor locations at a lower computational cost has been studied extensively in the literature. Early approaches include heuristics like cross entropy optimization (Naeem *et al.*, 2009), genetic algorithms (Yao *et al.*, 1993), and tabu search (Lau *et al.*, 2008). However, these heuristics neither provide any performance bounds nor do they guarantee convergence to the optimal solution. Joshi and Boyd (Joshi and Boyd, 2008) formulated the sensor selection problem as a non-convex optimization of the determinant of the error covariance matrix and proposed to solve a convex relaxation of it. They also provided a lower bound on the performance which can be used to find out how suboptimal the solution is. It has been found that due to the convex relaxation, this method sometimes results in an ill-conditioned matrix, especially when the number of sensors is limited. Few greedy approaches have also been proposed based on proxies of the estimation error like condition number (Astrid *et al.*, 2008; Willcox, 2006) and frame potential (Ranieri *et al.*, 2014). However, these proxies may also result in an ill-conditioned matrix. Moreover, minimizing these proxies results in the optimal solution only if the rows of the system matrix (observation vectors) are unit norm. Jiang et al. proposed MPME (Maximal Projection on Minimum Eigenspace) (Jiang *et al.*, 2016), a greedy sensor selection algorithm that maximizes the minimum eigenvalue of the system matrix in a computationally efficient manner. MPME outperforms condition number and frame potential based methods (in terms of the mean squared error), and can also guarantee that the sys-

tem matrix is well-conditioned. Further, it does not assume that the observation vectors are unit norm. These advantages make MPME a suitable algorithm for our problem.

Preliminary investigations have shown that MPME samples reduce the error to almost half the error obtained from random samples. For the simulation setup in Fig. 3.2, for an SR of 0.55 and SNR of 25dB, random samples gave an error of $\Delta_G = 12\%$ and $\Delta_T = 22\%$. In contrast, the same number of MPME samples gives an error of $\Delta_G = 5\%$ and $\Delta_T = 12\%$. Further investigation is needed to quantify the performance of the MPME sampling scheme.

4.1.2 Incident Field Expansion

One of the limitations of the method described in this thesis is that it assumes prior knowledge of the source distribution or the incident field. However, in many cases this information is not known. Therefore, a field prediction scheme that does not assume the knowledge of the incident field would be more practical and more widely applicable. Here, we present one of the ways of achieving this.

The incident field $\phi_i(\vec{r})$ is written as (see derivation of Eq. (2.8) in Chapter 1):

$$\phi_i(\vec{r}) = -j\omega\mu_0 \int_{V_i} g(\vec{r},\vec{r}\,')J(\vec{r}\,')dV' \tag{4.1}$$

where V_i is the region (centered at $\vec{r}_0$, and enclosing the source, and $g(\vec{r},\vec{r}\,') = -(j/4)H_0^{(2)}(k_0|\vec{r}-\vec{r}\,'|)$. The primed coordinates represent the variables of integration and lie within V_i. Using the Graf's Addition Theorem (Abramowitz and Stegun, 1948), we can expand the Hankel function as:

$$H_0^{(2)}(\eta|p\vec{r}_j|) = \sum_{n=-\infty}^{\infty} H_n^{(2)}(\eta|\vec{R}_{jl}|)J_n(\eta|\vec{r}_l|)e^{jn(\pi-\theta_l+\theta_{jl})} \tag{4.2}$$

where $\vec{R}_{jl} = \vec{r}_l - \vec{r}_j$ is the vector from $\vec{r}_j$ to $\vec{r}_l$; θ_l and θ_{jl} are the azimuth angles of $\vec{r}_l$ and $\vec{R}_{jl}$ respectively. Note that Equation (4.2) is valid only for $|\vec{r}_l| < |\vec{R}_{jl}|$.

By setting $\vec{r}_j = \vec{r} - \vec{r}\,'$, $\vec{r}_l = \vec{r}_0 - \vec{r}\,'$ and $\vec{R}_{jl} = \vec{r}_l - \vec{r}_j = \vec{r}_0 - \vec{r}$ in Eq. (4.2), and

substituting it in Eq. (4.1) we get:

$$\phi_i(\vec{r}) = -\frac{\omega\mu_0}{4}\int_{V_i}\Big(\sum_{n=-\infty}^{\infty} H_n^{(2)}(k_0|\vec{r}_0 - \vec{r}|)J_n(k_0|\vec{r}_0 - \vec{r}'|)e^{jn(\pi-\theta_l+\theta_{jl})}\Big)J(\vec{r}')dV', \tag{4.3}$$

Notice that $\vec{R}_{jl}$ and therefore θ_{jl} are independent of $\vec{r}'$. Also the condition $|\vec{r}_l| < |\vec{R}_{jl}|$ is trivially satisfied as long as $\vec{r}' \in V_i$ and $\vec{r} \notin V_i$.

Since the integral is on primed coordinates, we can simplify this equation further as follows:

$$\phi_i(\vec{r}) = \sum_{n=-\infty}^{\infty} \underbrace{\Big((-1)^{n+1}\frac{\omega\mu_0}{4}e^{jn\theta_{jl}}H_n^{(2)}(k_0|\vec{r}_0 - \vec{r}|)\Big)}_{s_n(\vec{r})} \overbrace{\int_{V_i} J_n(k_0|\vec{r}_0 - \vec{r}'|)e^{-jn\theta_l}J(\vec{r}')dV'}^{c_n} \tag{4.4}$$

Here, we have expanded the incident field in an infinite series in which c_n is the unknown and their corresponding coefficients $s_n(\vec{r})$ are calculated in closed form. When the source lies within a circular region of radius ρ, the infinite summation in Eq. (4.4) can be truncated to $\lceil 2k_0a + 1 \rceil$ terms (Bucci *et al.*, 1998) so that:

$$\phi_i(\vec{r}) \approx \sum_{n=-\lceil k_0a \rceil}^{\lceil k_0a \rceil} s_n(\vec{r})c_n \tag{4.5}$$

We can now substitute Eq. (4.5) in Eqs. (2.10) and (2.15), and solve for the incident field coefficients c_n along with the tangential field coefficients. Numerical experiments to verify the above derivation are left as future work.

4.1.3 Phaseless Recovery

In many situations, it is inconvenient (and sometimes impractical) to make measurements with phase. So, it becomes important to study reconstruction algorithms which work with phaseless (amplitude-only) data. In this case, the data equation takes the form $\boldsymbol{b} = |\boldsymbol{A}_p\boldsymbol{x}|$, where $\boldsymbol{b}$ is now real-valued ($|\cdot|$ denotes an element-wise modulus). The state equation remains the same as it does not depend on the measurements. The problem of recovering $\boldsymbol{x}$ from phaseless measurements is called 'Phase Retrieval' and has been studied extensively in the literature (Netrapalli *et al.*, 2013; Candes *et al.*, 2015*a*;

Jaganathan *et al.*, 2015; Sun *et al.*, 2018). Since it is a non-convex and an ill-posed problem, solving this is more challenging. Since the solution to any phase retrieval problem always has a constant global phase ambiguity, it is sufficient to consider a prediction of the field magnitude only.

One of the earliest applications of phase retrieval was in fields like Optics (Walther, 1963; Gonsalves, 1982) and X-Ray crystallography (Millane, 1990; Saldin *et al.*, 2001) where it was only possible to take phaseless measurements. Traditionally, an alternating projections approach has been taken to solve these problems (Gerchberg and Saxton, 1972; Fienup, 1982). However these approaches do not guarantee global convergence and may reach a local minima. One of the successful approaches in recent times is PhaseLift (Candes *et al.*, 2013) in which the unknown signal is lifted to a higher dimension (from N to N^2) and a semidefinite programming approach is then taken to solve the problem. PhaseLift requires at least $M = \mathcal{O}(N \log(N))$ measurements to converge to the correct solution. Due to the 'lift' to a higher dimension, PhaseLift is computationally demanding and infeasible for large signals. Another popular method is a gradient based method called the Wirtinger Flow algorithm (Candes *et al.*, 2015*b*). In this method, the initial estimate is obtained by means of a spectral method and it can be shown that for i.i.d. gaussian random measurements, this method converges locally with a high probability, requiring $(O(N \log(N)^2)$ measurements for phase recovery. Thus, both approaches require more measurements than the dimension of the unknown signal.

Naturally, if some a priori information is provided, it should be possible to reduce the number of measurements required. Compressive sensing provides a framework to incorporate this information, and a few methods have been suggested (Ohlsson *et al.*, 2011; Jaganathan *et al.*, 2012) for phase retrieval of sparse signals from fewer measurements than those required by the other methods mentioned above. Compressive Phase Retrieval via Lifting (CPRL— see (Ohlsson *et al.*, 2011)) has the same objective function as PhaseLift except there is an additional $l1$ minimization term due to which it can recover a k-sparse signal from $M = \mathcal{O}(k^2 \log(4N/k^2))$ measurements. For a signal of sufficient sparsity, CPRL requires lesser number of measurements than the number of components in the vector (N). Dictionary learning approaches further leverage the fact that even though a signal is not sparse in the original domain, it might admit a sparse representation in another basis or dictionary. DOLPHIn (Tillmann *et al.*, 2016) is one such algorithm for oversampled phase retrieval and involves iteratively updating the

signal, sparse codes and dictionary to arrive at the result. Tianyu Qiu et al. in (Qiu and Palomar, 2017) have proposed a dictionary learning algorithm SC-PRIME for undersampled measurements, i.e. $M < N$ using the majorization-minimization framework. However, one of the disadvantages of dictionary learning methods is the high sensitivity to algorithm hyperparameters, which are usually chosen heuristically. FASPR (Shi *et al.*, 2018) which is based on the total variation function (assuming the signal to have a sparse spatial gradient) addresses the problem of having to choose the hyperparameters heuristically by adaptively updating them.

However, none of these algorithms can be directly applied to our problem. This is because, in addition to the (phaseless) data equation, we have additionally the state equation. Therefore, a new phase retrieval algorithm has to be designed for this purpose.

4.1.4 Extensions to three dimensional geometries

In the current thesis, we only consider 2D scenarios. Extending our results to three dimensional (3D) geometries is one of the top-priority extensions of our current work. In the present work we restrict ourselves to 2D geometries for the following reasons:

1. In the process of this work — of solving the inverse problem in 2D — we have come across several nontrivial aspects of study which we believe is of general interest to the electromagnetics, signal processing, and inverse problems community.

2. To the best of our knowledge, the problem setup considered in our work is a first of a kind, with previous attempts being focused on ray-tracing approaches. As such, due to a lower computational load, it is possible to explore many directions within this framework, such as strategies to find optimal field measurement points, or investigating the impact of disturbance caused to the field by the field measuring entity (such as an unmanned vehicle). Such investigations will become computationally very cumbersome in 3D.

3. Now that the methodology of solving the problem in 2D has been established, going to 3D is straightforward. Technical difficulties aside, we do not anticipate any new conceptual challenges in this regard. Thus many of the essential aspects of the inverse problem are conveniently explored within the 2D setup.

4.2 Summary of the thesis

In this thesis, a surface integral based method for the prediction of EM fields was presented. The approach relies on the Huygens' principle and the Extinction theorem to represent the EM field measurements in the scattering environment in terms of the tangential fields on the surfaces of the scatterers. This problem was then posed as a convex optimization problem. A Subspace optimization based algorithm, CS-SOM was presented to solve for the tangential fields on the scatterers. Numerical results were presented to show the successful reconstruction of the tangential fields and the EM fields. It was shown that for an SR of 0.55 and an SNR of 25dB, the tangential fields are recovered with an average error of 22% and the EM fields on a grid are recovered with an error of 12%. Finally, a comparison of CS-SOM with other popular methods in the literature was presented.

REFERENCES

1. **Abramowitz, M.** and **I. A. Stegun**, *Handbook of mathematical functions with formulas, graphs, and mathematical tables*, volume 55. US Government printing office, 1948.

2. **Astrid, P.**, **S. Weiland**, **K. Willcox**, and **T. Backx** (2008). Missing point estimation in models described by proper orthogonal decomposition. *IEEE Transactions on Automatic Control*, **53**(10), 2237–2251.

3. **Balanis, C. A.**, *Advanced engineering electromagnetics*. John Wiley & Sons, 1999.

4. **Bose, A.** and **C. H. Foh**, A practical path loss model for indoor wifi positioning enhancement. *In Information, Communications & Signal Processing, 2007 6th International Conference on*. IEEE, 2007.

5. **Bucci, O. M.**, **C. Gennarelli**, and **C. Savarese** (1998). Representation of electromagnetic fields over arbitrary surfaces by a finite and nonredundant number of samples. *IEEE Transactions on Antennas and Propagation*, **46**(3), 351–359.

6. **Candes, E. J.**, **Y. C. Eldar**, **T. Strohmer**, and **V. Voroninski** (2015*a*). Phase retrieval via matrix completion. *SIAM review*, **57**(2), 225–251.

7. **Candes, E. J.**, **X. Li**, and **M. Soltanolkotabi** (2015*b*). Phase retrieval via wirtinger flow: Theory and algorithms. *IEEE Transactions on Information Theory*, **61**(4), 1985–2007.

8. **Candes, E. J.**, **T. Strohmer**, and **V. Voroninski** (2013). Phaselift: Exact and stable signal recovery from magnitude measurements via convex programming. *Communications on Pure and Applied Mathematics*, **66**(8), 1241–1274.

9. **Candes, E. J.**, **M. B. Wakin**, and **S. P. Boyd** (2008). Enhancing sparsity by reweighted l 1 minimization. *Journal of Fourier analysis and applications*, **14**(5-6), 877–905.

10. **Chen, X.** (2009). Subspace-based optimization method for solving inverse-scattering problems. *IEEE Transactions on Geoscience and Remote Sensing*, **48**(1), 42–49.

11. **Chen, X.**, *Computational methods for electromagnetic inverse scattering*. Wiley Online Library, 2018.

12. **Chew, W. C.**, *Waves and fields in inhomogeneous media*. IEEE Press Series on Electromagnetic Waves. IEEE Press, New York, 1995.

13. **Degli-Esposti, V.**, **D. Guiducci**, **A. de'Marsi**, **P. Azzi**, and **F. Fuschini** (2004). An advanced field prediction model including diffuse scattering. *IEEE Transactions on Antennas and Propagation*, **52**(7), 1717–1728.

14. **Fienup, J. R.** (1982). Phase retrieval algorithms: a comparison. *Applied optics*, **21**(15), 2758–2769.

15. **Gerchberg, R.** and **W. Saxton** (1972). A practical algorithm for the determination of the phase from image and diffraction plane pictures. *Optik*, **35**, 237.

16. **Glisson, A. W.**, **D. Kajfez**, and **J. James** (1983). Evaluation of modes in dielectric resonators using a surface integral equation formulation. *IEEE transactions on microwave theory and techniques*, **31**(12), 1023–1029.

17. **Gonsalves, R. A.** (1982). Phase retrieval and diversity in adaptive optics. *Optical Engineering*, **21**(5), 215829.

18. **Hansen, T. B.**, **R. A. Marr**, **U. H. Lammers**, **T. J. Tanigawa**, and **R. V. McGahan** (2006). Bistatic rcs calculations from cylindrical near-field measurements—part i: Theory. *IEEE transactions on antennas and propagation*, **54**(12), 3846–3856.

19. **Jaganathan, K.**, **Y. C. Eldar**, and **B. Hassibi** (2015). Phase retrieval: An overview of recent developments. *arXiv preprint arXiv:1510.07713*.

20. **Jaganathan, K.**, **S. Oymak**, and **B. Hassibi**, Recovery of sparse 1-d signals from the magnitudes of their fourier transform. *In 2012 IEEE International Symposium on Information Theory Proceedings*. IEEE, 2012.

21. **Ji, Z.**, **B.-H. Li**, **H.-X. Wang**, **H.-Y. Chen**, and **T. K. Sarkar** (2001). Efficient ray-tracing methods for propagation prediction for indoor wireless communications. *IEEE Antennas and Propagation Magazine*, **43**(2), 41–49.

22. **Jiang, C.**, **Y. C. Soh**, and **H. Li** (2016). Sensor placement by maximal projection on minimum eigenspace for linear inverse problems. *IEEE Transactions on Signal Processing*, **64**(21), 5595–5610.

23. **Joshi, S.** and **S. Boyd** (2008). Sensor selection via convex optimization. *IEEE transactions on Signal Processing*, **57**(2), 451–462.

24. **Kajfez, D.**, **A. W. Glisson**, and **J. James** (1984). Computed modal field distributions for isolated dielectric resonators. *IEEE transactions on Microwave Theory and Techniques*, **32**(12), 1609–1616.

25. **Lau, S.**, **R. Eichardt**, **L. Di Rienzo**, and **J. Haueisen** (2008). Tabu search optimization of magnetic sensor systems for magnetocardiography. *IEEE Transactions on Magnetics*, **44**(6), 1442–1445.

26. **Liu, Y.**, **S. Safavi-Naeini**, **S. K. Chaudhuri**, and **R. Sabry** (2004). On the determination of resonant modes of dielectric objects using surface integral equations. *IEEE Transactions on Antennas and Propagation*, **52**(4), 1062–1069.

27. **Massa, A.**, **P. Rocca**, and **G. Oliveri** (2015). Compressive sensing in electromagnetics-a review. *IEEE Antennas and Propagation Magazine*, **57**(1), 224–238.

28. **Millane, R. P.** (1990). Phase retrieval in crystallography and optics. *JOSA A*, **7**(3), 394–411.

29. **Mitzner, K.**, Numerical solution of the exterior scattering problem at eigenfrequencies of the interior problem. *In Radio Union Meeting, Boston, Mass*. 1968.

30. **Mongia, R. K.** and **A. Ittipiboon** (1997). Theoretical and experimental investigations on rectangular dielectric resonator antennas. *IEEE Transactions on Antennas and Propagation*, **45**(9), 1348–1356.

31. **Morozov, V.** and **A. Grebennikov**, *Methods for solution of Ill-posed problems: algorithmic aspects*. Moscow univ. press Moscow, 2005.

32. **Naeem, M.**, **S. Xue**, and **D. Lee**, Cross-entropy optimization for sensor selection problems. *In 2009 9th International Symposium on Communications and Information Technology*. IEEE, 2009.

33. **Netrapalli, P.**, **P. Jain**, and **S. Sanghavi**, Phase retrieval using alternating minimization. *In* **C. J. C. Burges**, **L. Bottou**, **M. Welling**, **Z. Ghahramani**, and **K. Q. Weinberger** (eds.), *Advances in Neural Information Processing Systems 26*. Curran Associates, Inc., 2013, 2796–2804. URL `http://papers.nips.cc/paper/5041-phase-retrieval-using-alternating-minimization.pdf`.

34. **Ohlsson, H.**, **A. Y. Yang**, **R. Dong**, and **S. S. Sastry** (2011). Compressive phase retrieval from squared output measurements via semidefinite programming. *arXiv preprint arXiv:1111.6323*, 1–27.

35. **Pei, L.**, **R. Chen**, **J. Liu**, **H. Kuusniemi**, **T. Tenhunen**, and **Y. Chen** (2010). Using inquiry-based bluetooth rssi probability distributions for indoor positioning. *Journal of Global Positioning Systems*, **9**(2), 122–130.

36. **Qiu, T.** and **D. P. Palomar** (2017). Undersampled sparse phase retrieval via majorization–minimization. *IEEE Transactions on Signal Processing*, **65**(22), 5957–5969.

37. **Ranieri, J.**, **A. Chebira**, and **M. Vetterli** (2014). Near-optimal sensor placement for linear inverse problems. *IEEE Transactions on signal processing*, **62**(5), 1135–1146.

38. **Remley, K. A.**, **H. R. Anderson**, and **A. Weisshar** (2000). Improving the accuracy of ray-tracing techniques for indoor propagation modeling. *IEEE transactions on vehicular technology*, **49**(6), 2350–2358.

39. **Saldin, D.**, **R. Harder**, **V. Shneerson**, and **W. Moritz** (2001). Phase retrieval methods for surface x-ray diffraction. *Journal of Physics: Condensed Matter*, **13**(47), 10689.

40. **Sanghvi, Y.**, **Y. N. G. B. Kalepu**, and **U. Khankhoje** (2019). Embedding deep learning in inverse scattering problems. *IEEE Transactions on Computational Imaging*.

41. **Sastry, D. K.**, **C. Bhat**, and **U. K. Khankhoje**, Spatial prediction of undersampled electromagnetic fields. *In 2019 PhotonIcs & Electromagnetics Research Symposium-Spring (PIERS-Spring)*. IEEE, 2019.

42. **Shi, B.**, **S. Chen**, **Y. Tian**, **X. Fan**, and **Q. Lian** (2018). Faspr: A fast sparse phase retrieval algorithm via the epigraph concept. *Digital Signal Processing*, **80**, 12–26.

43. **Sun, J.**, **Q. Qu**, and **J. Wright** (2018). A geometric analysis of phase retrieval. *Foundations of Computational Mathematics*, **18**(5), 1131–1198.

44. **Tillmann, A. M.**, **Y. C. Eldar**, and **J. Mairal** (2016). Dolphin—dictionary learning for phase retrieval. *IEEE Transactions on Signal Processing*, **64**(24), 6485–6500.

45. **Toscano, A.**, **F. Bilotti**, and **L. Vegni** (2003). Fast ray-tracing technique for electromagnetic field prediction in mobile communications. *IEEE transactions on magnetics*, **39**(3), 1238–1241.

46. **Walther, A.** (1963). The question of phase retrieval in optics. *Optica Acta: International Journal of Optics*, **10**(1), 41–49.

47. **Wei, Z.**, **R. Chen**, **H. Zhao**, and **X. Chen** (2016). Two fft subspace-based optimization methods for electrical impedance tomography. *Progress In Electromagnetics Research*, **157**, 111–120.

48. **Willcox, K.** (2006). Unsteady flow sensing and estimation via the gappy proper orthogonal decomposition. *Computers & fluids*, **35**(2), 208–226.

49. **Wu, Z.-H.**, **Y. Han**, **Y. Chen**, and **K. R. Liu** (2015). A time-reversal paradigm for indoor positioning system. *IEEE Transactions on Vehicular Technology*, **64**(4), 1331–1339.

50. **Yao, L.**, **W. A. Sethares**, and **D. C. Kammer** (1993). Sensor placement for on-orbit modal identification via a genetic algorithm. *AIAA journal*, **31**(10), 1922–1928.

LIST OF PAPERS BASED ON THESIS

1. Chandan Bhat†, Karteekeya Sastry†, and Uday K. Khankhoje. "Compressive sensing approaches for prediction of scattered electromagnetic fields." *Journal of the Optical Society of America A (JOSA A)*; 37 (7), 2020.

   † *These authors contributed equally to this work*

2. Karteekeya Sastry, Chandan Bhat, and Uday K. Khankhoje. "Spatial Prediction of Undersampled Electromagnetic Fields." *2019 PhotonIcs & Electromagnetics Research Symposium-Spring (PIERS-Spring)*, IEEE, 2019.

Compressive sensing approaches for prediction of scattered electromagnetic fields

CHANDAN BHAT†, KARTEEKEYA SASTRY† AND UDAY K KHANKHOJE

Department of Electrical Engineering, Indian Institute of Technology Madras, Chennai, India.
† *These authors contributed equally to this work*

We present a novel method based on Huygens' principle and compressive sensing to predict the electromagnetic (EM) fields in arbitrary scattering environments by making a few measurements of the field. In doing so, we assume a homogeneous medium between the scatterers, though we do not assume prior knowledge of the permittivities or the exact geometry of the scatterers. The major contribution of this work is a compressive sensing based subspace optimization method (CS-SOM). Using this, we show that the EM fields in an indoor situation with upto four scattering object can be reconstructed with approximately 12% error, when the number of measurements is only 55% of the number of variables used to formulate the problem. Our technique departs significantly from traditional ray tracing approaches. We use a surface integral formulation which captures wave-matter interactions exactly, leverage compressive sensing techniques so that field measurements at a few random locations suffice, and apply Huygens' principle to predict the fields at any location in space.

OCIS codes: (110.0110) Imaging systems; (110.1758) Computational Imaging;(100.3200) Inverse Scattering

http://dx.doi.org/10.1364/ao.XX.XXXXXX

1. INTRODUCTION

Reconstruction of electromagnetic (EM) fields in a scattering environment is a fundamental problem, with many practical applications such as radar cross-section estimation [1], indoor positioning [2, 3], Wi-Fi access point planning [4] and such others. Traditional approaches to this problem use ray tracing methods [5–7]. These techniques are valid only in the high frequency regime, suffer from large errors in near-field estimation, and face difficulties in modelling multiple scattering events [Fig. 3 8]. These drawbacks may limit their applicability significantly. In this paper, we overcome these limitations by proposing new techniques that model wave-matter interactions exactly using surface integral formulations. This characterization enables accurate prediction of EM fields in *arbitrary* scattering environments.

Problem statement: The general real-world problem that we aim to address is as follows: Consider a room with some objects such as tables and chairs in which an active antenna (e.g. a Wi-Fi router) is placed. Can the electromagnetic field at every point inside the room be predicted?

It is desirable to solve this problem by making the least possible number of field measurements. For this reason, interpolation based techniques are impractical because field variations on a sub-wavelength scale dictate a high density of measurements. Motivated by this, we present techniques that can reconstruct fields by making few measurements. A major strength of our approach is that we do not need to know the permittivity of the objects; only a rough estimate of their locations is sufficient. That said, we assume that the medium between the scatterers is homogeneous. An abstraction of the real world problem stated above is shown schematically in Fig. 1 by means of a two-dimensional (2D) scattering problem.

Our approach: According to Huygens' principle, the scattered field at a point can be expressed as a convolution between the free space Green's function and the tangential electric and magnetic fields on the surface of the scatterers. Additionally, the Extinction theorem enforces certain relations between the tangential electric and magnetic fields [9]. Thus, estimating these tangential fields by using the above relations points the way to predicting the scattered fields outside the scattering objects. Further, it is empirically observed that these tangential fields are sparse in certain bases (we substantiate this later in the text). By leveraging this prior information and using the theory of compressive sensing, we can bring down the number of measurements required.

In the discrete world, the relation between the measurements, $\boldsymbol{b} \in \mathbb{C}^M$, and the tangential fields, $\boldsymbol{x} \in \mathbb{C}^N$, is given by the system matrix, A, as $\boldsymbol{b} = A\boldsymbol{x} + \boldsymbol{\nu}$, where $\boldsymbol{\nu}$ represents measurement noise, M is the number of measurements, and N the number of variables used to describe the tangential fields. Additionally, the Extinction theorem gives the following relation between the tangential fields: $A_s\boldsymbol{x} = \boldsymbol{b}_s$, where $\boldsymbol{b}_s \in \mathbb{C}^{N/2}$ contains the incident field, and A_s is termed as the state matrix. The field

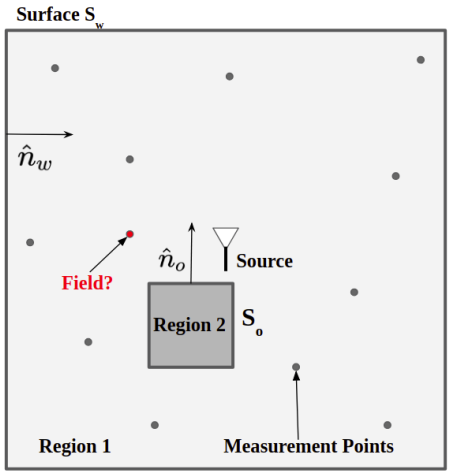

Fig. 1. Schematic of the problem statement: Can the field be predicted anywhere in Region 1 (a homogeneous medium) by making a few measurements in the presence of an obstacle denoted by Region 2? S_w is the inner surface of the enclosing wall and S_o is the outer surface of the scatterer. $\hat{n}_w$ and $\hat{n}_o$ are normals to the scattering surfaces of the wall and object, respectively.

predicted, $\boldsymbol{f} \in \mathbb{C}^S$, is expressed in terms of the prediction matrix B, as $\boldsymbol{f} = B\boldsymbol{x}$, where S is the number of locations where the field is desired. Therefore, the problem boils down to estimating $\boldsymbol{x}$ given $\{\boldsymbol{b}, \boldsymbol{b}_s\}$ which is a convex optimization problem with known solution strategies [10, 11].

The problem of recovering a higher dimensional signal from lower dimensional field measurements has been widely studied in the inverse imaging community[12–14]. In particular, a family of so-called subspace optimization methods (SOM) [15] provide a convenient framework to split the desired signal into two orthogonal subspaces, and to independently recover each component. In recent work [16], we have shown an efficient scheme to recover one component from the field data, and the other based on a priori information.

Our contributions: To the best of our knowledge, this approach of using the surface integral formulation along with compressive sensing for solving the problem of field prediction has not been reported earlier. We propose a compressive sensing-based subspace optimization method (CS-SOM), that works by splitting a signal into two orthogonal vector subspaces and uses signal sparsity in suitable domains to realize high accuracy field predictions. Using this technique, we show that in a scattering environment (such as in the schematic of Fig. 1), the EM field (in Region 1) can be reconstructed with approximately 12% error and the tangential fields on scatterer surfaces can be reconstructed with approximately 22% error, when the number of measurements is only 55% of the number of variables used to formulate the problem.

Paper organization: The rest of the paper is organised as follows. We formally define the problem statement in Section 2. Then, Section 3 explains the theoretical details of the CS-SOM algorithm used to solve the stated problem. Numerical Results for the field prediction are presented in Section 4. We conclude with a discussion of open issues, limitations, and possible applications of our techniques in Section 5.

2. PROBLEM FORMULATION

Governing Physics: The electromagnetic (EM) field at any location can be obtained using Huygens' principle, which states that the field at any location is the superposition of primary (incident fields) and secondary sources located on scatterer surface(s) (scattered fields) [9]. The schematic shown in Fig. 1 shows a two dimensional (2D) computational domain which is illuminated by a transverse magnetic (TM) polarization field. The $z-$component of the electric field in Region 1, $\phi(\vec{r})$, can be expressed using Huygens' principle [17] as:

$$\begin{aligned}\phi(\vec{r}) &= \phi_{in}(\vec{r}) \\ &- \oint_{S_w} [g(\vec{r},\vec{r}')\nabla'\phi_w(\vec{r}') - \phi_w(\vec{r}')\nabla' g(\vec{r},\vec{r}')] \cdot \hat{n}_w \, dl' \\ &- \oint_{S_o} [g(\vec{r},\vec{r}')\nabla'\phi_o(\vec{r}') - \phi_o(\vec{r}')\nabla' g(\vec{r},\vec{r}')] \cdot \hat{n}_o \, dl', \end{aligned} \quad \textbf{(1)}$$

where $g(\vec{r},\vec{r}') = -(j/4)H_0^{(2)}(k_0|\vec{r}-\vec{r}'|)$ is the free space Green's function in Region 1, $\phi_{in}(\vec{r})$ is the incident electromagnetic field due to a source, ϕ_o, ϕ_w are the tangential electric fields on the object and wall surfaces, and $\hat{n}_w$ and $\hat{n}_o$ are normals to the scattering surfaces of the wall and object, respectively, as shown in Fig. 1. It can be shown that $\nabla\phi_o \cdot \hat{n}_o$ and $\nabla\phi_w \cdot \hat{n}_w$ are proportional to the tangential magnetic fields on the object and wall, respectively. S_w is the inner surface of the enclosing wall and S_o is the surface of the scatterer; since the problem is 2D, the surface integrals are equivalent to contour integrals.

As per the Uniqueness theorem of electromagnetics [9], it is superfluous to use *both* the tangential electric and magnetic fields over the entire surfaces to determine the field when using Huygens' principle. Indeed, the tangential electric and magnetic fields on the surface are related to themselves via the Extinction theorem. When we apply this theorem to Region 1, the following relation is obtained between the tangential field variables, $\{\phi_t(\vec{r}), \nabla\phi_t(\vec{r}) \cdot \hat{n}_t\}$, $t \in \{o, w\}$:

$$\begin{aligned}&- \oint_{S_w} [g(\vec{r},\vec{r}')\nabla'\phi_w(\vec{r}') - \phi_w(\vec{r}')\nabla' g(\vec{r},\vec{r}')] \cdot \hat{n}_w \, dl' \\ &- \oint_{S_o} [g(\vec{r},\vec{r}')\nabla'\phi_o(\vec{r}') - \phi_o(\vec{r}')\nabla' g(\vec{r},\vec{r}')] \cdot \hat{n}_o \, dl' \\ &= -\phi_{in}(\vec{r}), \quad \vec{r} \in \{S_w, S_o\}. \end{aligned} \quad \textbf{(2)}$$

Discretized equations: We express the unknowns ϕ_w, ϕ_o, $(\nabla\phi_w \cdot \hat{n}_w)$ and $(\nabla\phi_o \cdot \hat{n}_o)$ in a known basis $p_n(r)$, as:

$$\phi_o(r) = \sum_{i=1}^{N_o} a_n^o p_n(r), \qquad \nabla\phi_o(r) \cdot \hat{n}_o = \sum_{i=1}^{N_o} b_n^o p_n(r), \quad \textbf{(3)}$$

$$\phi_w(r) = \sum_{i=1}^{N_w} a_n^w q_n(r), \qquad \nabla\phi_w(r) \cdot \hat{n}_w = \sum_{i=1}^{N_w} b_n^w q_n(r), \quad \textbf{(4)}$$

where lowercase r is reserved to denote the parametrized distance along each respective surface (S_o or S_w); $p_i(r)$, $i = 1, 2, \ldots, N_o$, and $q_i(r)$, $i = 1, 2, \ldots, N_w$ are the sets of basis functions and a_n^o, b_n^o, a_n^w and b_n^w are the unknown coefficients. Substituting Eq. (3) and Eq. (4) in Eq. (1), and considering M locations of field measurement, we get a linear system of equations of the

following form:

$$\underbrace{\begin{bmatrix} E & F & G & H \end{bmatrix}}_{A} \underbrace{\begin{bmatrix} \boldsymbol{a}^o \\ \boldsymbol{b}^o \\ \boldsymbol{a}^w \\ \boldsymbol{b}^w \end{bmatrix}}_{\boldsymbol{x}} = \underbrace{\begin{bmatrix} \phi_s(\vec{r}_1) \\ \phi_s(\vec{r}_2) \\ \vdots \\ \phi_s(\vec{r}_M) \end{bmatrix}}_{\boldsymbol{b}} + \boldsymbol{\nu} \tag{5}$$

where $\{E, F\} \in \mathbb{C}^{M \times N_o}$, $\{G, H\} \in \mathbb{C}^{M \times N_w}$ compose the system matrix $A \in \mathbb{C}^{M \times N}$, $x \in \mathbb{C}^N$ is a vector with vertically stacked elements $\{\boldsymbol{a}^o, \boldsymbol{b}^o\} \in \mathbb{C}^{N_o}$ and $\{\boldsymbol{a}^w, \boldsymbol{b}^w\} \in \mathbb{C}^{N_w}$, with $N = 2(N_w + N_o)$ determining the total number of unknowns. The scattered field at a location $\vec{r}_i$ is $\phi_s(\vec{r}_i)$, which is corrupted by noise given in ν.

Similarly, substituting Eq. (3) and Eq. (4) in Eq. (2), gives the following form of the discretized "state" equation:

$$A_s \boldsymbol{x} = \underbrace{-\left[\phi_{in}(\vec{r}_1^{(s)}) \cdots \phi_{in}(\vec{r}_{\frac{N}{2}}^{(s)})\right]^T}_{\boldsymbol{b}_s}, \tag{6}$$

where $A_s \in \mathbb{C}^{\frac{N}{2} \times N}$ is the state matrix, and $\vec{r}_i^{(s)}$, $i \in [1, \frac{N}{2}]$ in this case refer to unique points along the surfaces S_o, S_w; these points are made precise once the choice of basis functions is made concrete.

One of the standard methods of *exactly* solving this linear system for the coefficients ϕ_w, ϕ_o, $(\nabla\phi_w \cdot \hat{n}_w)$ and $(\nabla\phi_o \cdot \hat{n}_o)$ is to combine the above equation with the Extinction theorem for the other regions (however, this requires knowledge of the scatterer permittivity), and then solve numerically by using the Method of Moments (MOM) [9].

Key Idea: Our approach is to trade off the exactness of the solution with the knowledge of the scatterer permittivity, there by only using Eqs. (5,6) to *estimate* the unknown coefficients. Recall that this only involves the Green's function for Region 1 (i.e. free space), whereas the exact solution requires the Green's function for both Regions. Typically, Region 1 will always be free space, whereas Region 2 will include objects with heterogeneous permittivity, usually unknown in practical situations.
The above mentioned estimation can be accomplished by measuring the field at a few random locations such that the right hand side vector $\boldsymbol{b}$ in Eq. (5) is known. Since the system matrix A has been constructed beforehand, the coefficients $\boldsymbol{x}$ can be estimated, and as a result, the tangential fields are known via Eqs. (3,4). Then, substituting these fields back in Eq. (1), we can predict the field at any point in Region 1.

Ideally we are interested in making this prediction by measuring the field at as few locations as required. This typically leads to the case of having the number of measurements, M, be less than the number of unknowns, N, i.e. A is under-determined. For this setup, the problem is formulated as follows,

1. Estimate the tangential fields by solving the following convex optimization problem:

$$\underset{\boldsymbol{x}}{\text{minimize}} \quad \|A\boldsymbol{x} - \boldsymbol{b}\|_2 \leq \epsilon, \ \|A_s\boldsymbol{x} - \boldsymbol{b}_s\|_2 \leq \eta \tag{7}$$

   where $A, A_s, \boldsymbol{x}, \boldsymbol{b}_s$ are as before, $\boldsymbol{b} \in \mathbb{C}^M$ is the vector containing noisy measurements, ϵ is an estimate of the square root of the noise variance, and η is an estimate of the discretization error in the state equation.

2. Substitute $\boldsymbol{x}$ from above into Eq. (1) and calculate the field at S locations. Let the true field at these S locations obtained from the forward solver be $\boldsymbol{f} \in \mathbb{C}^S$ (i.e. this data is generated synthetically). Then we compute the error, $e \in \mathbb{R}$ as

$$e = \|B\boldsymbol{x} - \boldsymbol{f}\|_2 \tag{8}$$

   where $B \in \mathbb{C}^{S \times N}$ is the matrix obtained from Huygens' principle Eq. (1), which when multiplied with the tangential fields $\boldsymbol{x}$ gives the estimates of the EM fields.

It is crucial to note that B is identical to A in structure; the difference arises purely due to the choice of the location $\vec{r}$ in the Green's function, $g(\vec{r}, \vec{r}')$; in A this $\vec{r}$ corresponds to measurement locations, whereas in B, it corresponds to the locations where the field is desired. Therefore, in order to construct B, we follow the same procedure described in this Section (Discretize Eq. (1) by expanding the unknowns in a suitable basis and plug in those values of $\vec{r}$ where the field prediction is desired). It is to be noted that we are interested in predicting the fields outside the object (i.e. in Region 1). To get the fields inside the objects we need to consider the Extinction theorem, which involves knowing the exact permittivities of the objects. Also note that even though in this paper we only deal with the scalar 2D case, extensions to the 3D case or to the vector formulation are not fundamentally different.

3. COMPRESSIVE SENSING BASED SUBSPACE OPTIMIZATION

In this Section, we explain the algorithm used to solve the problem formulated in the previous Section.

System & State matrix : The system matrix depends on a particular choice of the basis functions, $p_i(r)$, previously introduced. To represent the tangential fields on scatterer surfaces, we use pulse basis functions defined as follows: an arbitrarily shaped contour S of length L is divided into n segments of equal length, and with r denoting the parameterized distance along the contour (the starting point on the contour is chosen arbitrarily), the i^{th} basis function is:

$$p_i(r) = \begin{cases} 1 & r_{S,i-1} \leq r \leq r_{S,i} \\ 0 & \text{else} \end{cases} \qquad i \in [1, n],\ 0 \leq r \leq L$$

where $r_{S,i}$ denotes the parameterized distance giving the end of the i^{th} segment on S. In our case, the contour could be either the object S_o (with $n = N_o$, basis functions denoted by p), or the wall S_w (with $n = N_w$, basis functions denoted by q). In this pulse basis, the system matrix is denoted as $A_p = [E_p\ F_p\ G_p\ H_p]$, with the elements of each sub-matrix given by the corresponding lower-case symbols [18]:

$$\begin{aligned} e_{m,k} &= \int_{r_{w,k-1}}^{r_{w,k}} \frac{jk_0}{4\rho_{r_m}} H_1^{(2)}(k_0\rho_m)(\Delta\vec{R}_m \cdot \hat{n})\, dr \\ f_{m,k} &= -\int_{r_{w,k-1}}^{r_{w,k}} \frac{j}{4} H_0^{(2)}(k_0\rho_m)\, dr \\ g_{m,k} &= \int_{r_{o,k-1}}^{r_{o,k}} \frac{jk_0}{4\rho_{r_m}} H_1^{(2)}(k_0\rho_m)(\Delta\vec{R}_m \cdot \hat{n})\, dr \\ h_{m,k} &= -\int_{r_{o,k-1}}^{r_{o,k}} \frac{j}{4} H_0^{(2)}(k_0\rho_m)\, dr \end{aligned} \tag{9}$$

where $\Delta\vec{R}_m = \vec{R}_m - \vec{R}(r)$, $\rho_m = |\Delta\vec{R}_m|$ with $\vec{R}_m$ denoting the position vector of the m^{th} measurement point, and $\vec{R}(r)$ denoting the position vector of the point on the respective contour with

parameterized distance r. Similar expressions can be obtained for the elements of the state matrix by setting $\{\vec{r}_1^{(s)}, \ldots, \vec{r}_{\frac{N}{2}}^{(s)}\}$ in Eq. (6) to the midpoints of the discretized segments of the surfaces S_o and S_w (these segments are $\frac{N}{2}$ in number). Sufficient care has to be taken while evaluating the associated singular integrals.

Subspace Optimization Method In order to solve this problem we improvise on the subspace optimization method (SOM) [15], typically used in the context of inverse scattering problems. Here, the signal of interest is recovered from its projection in two orthogonal subspaces. Our approach begins with the singular value decomposition (SVD) of the system matrix as $A_p = \sum_i u_i \sigma_i v_i^H$, where u, v represent the left and right singular vectors and σ's are the corresponding singular values (with $\sigma_{i+1} \geq \sigma_i$). The essential idea is to consider the following orthogonal vector spaces, the 'signal' space spanned by the top L_o right singular vectors of the system matrix A_p, and the 'noise' space that is spanned by the remaining $N - L_o$ vectors. In the absence of noise, L_o would simply be the the number of independent rows of the matrix A_p, and the 'signal' and 'noise' subspaces would be identical to the row and null spaces of the matrix A_p, respectively. However, in the presence of noise, the lower singular values amplify the noise from the measurements and lead to a large error in the solution. Thus, the solution sought is expanded as $\boldsymbol{x} = \boldsymbol{x}_s + \boldsymbol{x}_n$, corresponding to the signal and noise spaces, respectively, which are estimated as follows:
(i) Signal space estimation: This component, $\boldsymbol{x}_s$, is determined by a L_o-term truncation of the SVD of A_p as follows:

$$\boldsymbol{x}_s = \sum_{i=1}^{L_o} \left(\frac{u_i^H b}{\sigma_i} \right) v_i.$$

An immediate question concerns the selection of the parameter L_o. This number is chosen using the Morozov discrepancy principle [19], where L_o is chosen as the smallest number such that $\|A_p \boldsymbol{x}_s - b\|_2 < \epsilon$, where ϵ is the variance of the noise, which in many situations, is reasonably known. The problem is not very sensitive to the exact choice of L_o, as the remaining components are determined in the next stage; various studies have also corroborated this observation [15, 16].
(ii) Noise space estimation: This component, $\boldsymbol{x}_n$ is determined from apriori information about the problem, based on the following observation: when the discrete Fourier transform (DFT) coefficients of the *true* tangential fields are computed (using a forward solver, see plots in Fig. 2), we observe that most of the coefficients are very low in magnitude, i.e. the solution exhibits sparsity in the DFT basis. This property can be exploited to reconstruct the EM fields by using ideas from Compressive Sensing [20] which penalizes the l_1 norm of the solution vector to promote sparse solutions. As per the rigourous requirements of Compressive Sensing, a sparse signal can be reconstructed from undersampled linear measurements provided that the sensing matrix follows the restrictive isometry property (RIP). Since the RIP is difficult to verify in practice, we heuristically apply Compressive Sensing ideas to our problem, a strategy that has gained popularity in the electromagnetics community [11] in recent times. Thus, holding $\boldsymbol{x}_s$ constant, the noise space estimation proceeds as per the following optimization problem:

$$\begin{aligned} \underset{\boldsymbol{x}_n}{\text{minimize}} \quad & \|M(\boldsymbol{x}_s + \boldsymbol{x}_n)\|_1 \\ \text{subject to} \quad & \|A_p \boldsymbol{x}_n - (\boldsymbol{b} - A_p \boldsymbol{x}_s)\|_2 \leq \epsilon, \\ & \|A_s \boldsymbol{x}_n - (\boldsymbol{b}_s - A_s \boldsymbol{x}_s)\|_2 \leq \eta \end{aligned} \tag{10}$$

where $M = \mathcal{F}, \mathcal{W}$, or $\mathcal{D}$ are the DFT, wavelet or DCT bases, respectively, chosen as candidates for sparse representations.

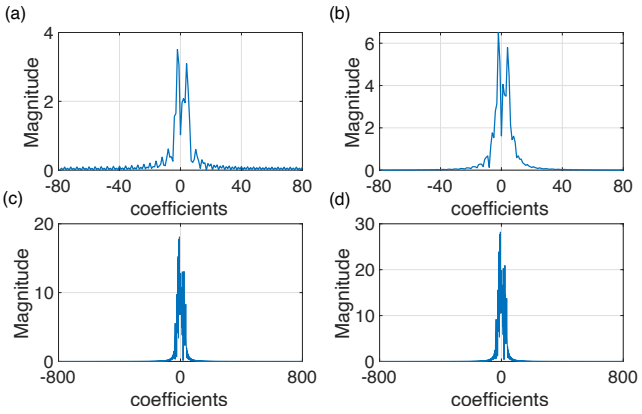

Fig. 2. DFT coefficients of the tangential fields (a) $\nabla \phi_o \cdot \hat{n}_o$, (b) ϕ_o on the scattering surface S_o and (c) $\nabla \phi_w \cdot \hat{n}_w$, (d) ϕ_w on the scattering surface S_w as shown in Fig. 1. Most coefficients have very low magnitudes.

4. NUMERICAL RESULTS

In this section we present the numerical results for the prediction of spatial electromagnetic fields from measurements using the formulations described previously. We describe the simulation setup, define the error metrics and then present the results for varying number of objects. All simulations are programmed in MATLAB 2018b and executed on an Intel Core i7-7700 CPU running at 3.60GHz, using 16GB RAM.

Simulation Setup: The simulation domain is $10\lambda \times 10\lambda$ with four objects all with different permittivities and an outer wall which encloses all the objects. The simulation setup is shown in Fig. 3 with objects 1,2,3 and 4 centered at $(-2.5\lambda, 1.5\lambda)$, $(2\lambda, 2\lambda)$, $(1\lambda, -2.5\lambda)$ and $(-2.5\lambda, -1\lambda)$ respectively, where λ is the wavelength; The relative permittivities of the objects 1, 2, 3, 4 and wall are $\epsilon_{r1} = 3.7 - 2.1j$, $\epsilon_{r2} = 1.7 - 1.1j$, $\epsilon_{r3} = 2.7 - 3.7j$, $\epsilon_{r4} = 1.2 - 1.1j$ and $\epsilon_{rw} = 3.7 - 2.1j$ respectively (lossy, so as to mimic real life materials such as a concrete wall, etc.). Object 1 is a square of side λ, object 2 is a cirle with radius 0.75λ, object 3 is a rectangle with sides $1\lambda \times 2.5\lambda$ and object 4 is a circle with radius 1λ. Note that the permittivity and the true geometry of the objects are used only in the forward solver to generate the synthetic measurements. The source is placed at the location $\vec{r}_0 = (0.5\lambda, -0.75\lambda)$, with a cylindrical plane wave of the form: $\phi_{inc}(\vec{r}) = H_0^{(2)}(k_0|\vec{r} - \vec{r}_0|)$.

We obtain the true fields first using the Boundary Integral (BI) method using pulse basis for the tangential fields on the surface of the scatterers. Substituting the true tangential fields in Huygens' principle (Eq. (1)), fields at all other locations are obtained. For this problem, a spatial discretization of $\lambda/40$ is considered to ensure numerical convergence. To verify the correctness of our forward solver, we have simulated the scattering from a single infinite cylinder of radius λ and validated it with the Mie series solution, finding agreement within a relative error of 1.5%. Since the electric field integral equation is known to display numerical issues related to cavity resonances, we verify (numerically) that there are no resonances in the frequency range $f_0 \pm \frac{f_0}{3}$, where f_0 is the operating frequency in our simulations.

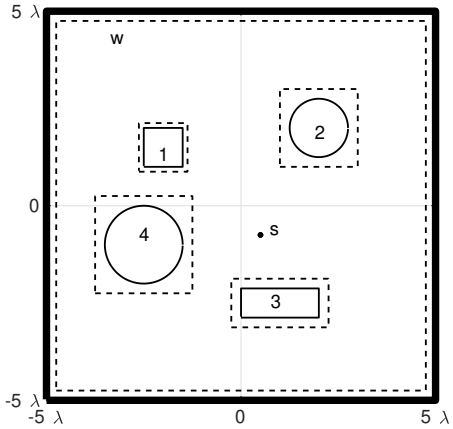

Fig. 3. The schematic of $10\lambda \times 10\lambda$ simulation domain. The domain includes a wall, 4 objects and a source. The objects 1,2,3 and 4 have their centers respectively at $(-2.5\lambda, 1.5\lambda)$, $(2\lambda, 2\lambda)$, $(1\lambda, -2.5\lambda)$ and $(-2.5\lambda, -1\lambda)$. The source is located at $(0.5\lambda, -0.75\lambda)$ and 'w' is the outer boundary. The dotted contours are the approximate geometry of the objects used in the field reconstruction algorithm.

The measurements are corrupted with additive white Gaussian noise (AWGN) with a signal to noise ratio (SNR) of 25 dB and 10 dB.

Error metric definition: We define two error metrics in order to evaluate the performance of our method, namely the tangential field error, (Δ_T), and the error in reconstruction on the 2D grid (Δ_G). The tangential field error is defined as,

$$\Delta_T = \frac{\|\boldsymbol{x}_{est} - \boldsymbol{x}_{true}\|_2}{\|\boldsymbol{x}_{true}\|_2} \tag{11}$$

where $\boldsymbol{x}_{est}$ and $\boldsymbol{x}_{true}$ are the estimated and true tangential fields respectively.

For the purpose of quantifying the accuracy of the predicted field, the field is estimated over the $10\lambda \times 10\lambda$ region that is discretized on a grid with pitch equal to $\lambda/20$.

The error in reconstruction is calculated using the following relation:

$$\text{error } (\Delta_G) = \frac{\|\phi_{est} - \phi_{true}\|_2}{\|\phi_{true}\|_2} \tag{12}$$

where ϕ_{est} and ϕ_{true} are the estimated and true fields over the 2D grid of points respectively.

We also define the relative error at a location $\vec{r}$ as:

$$\frac{|\phi_{est}(\vec{r}) - \phi_{true}(\vec{r})|}{|\phi_{true}(\vec{r})|} \tag{13}$$

where $\phi_{est}(\vec{r})$ and $\phi_{true}(\vec{r})$ are the estimated and true fields at $\vec{r}$ respectively.

The fields inside the object and fields that are very close to the scatterer surfaces (at a distance less than $\lambda/10$ from the approximate surfaces of the objects) are not considered in the error calculation.

Problem Discretizations: For predicting the field we don't assume the knowledge of the exact shape of the scatterer, instead we approximate the geometry of the object by a bounding box that encloses the object. This is shown in Fig. 3 by means of dotted contours around the objects. The system matrix and the state matrix for the inverse problem (of the form given in Eq. (9) are obtained using a uniform discretization of $\lambda/5$ along the dotted contours. This was chosen heuristically based on numerical experiments where the discretization was varied from $\lambda/2$ to $\lambda/20$; it was found that a discretization of $\lambda/5$ gives the optimal trade-off between accuracy and computational cost. The number of unknowns for the tangential fields varies with the number of objects; considering all four objects and the wall, there are 704 unknowns. In the figures shown below, we consider the case of all 4 objects and the wall with 387 randomly chosen field measurements (0.55 times the number of unknowns) with 25 dB SNR. The system matrix A_p has a rank of 380, and using the Morozov principle gives a number L_o in the range of 140-150 as the number of significant singular values at this value of SNR (i.e the signal space is spanned by the first L_o right singular vectors of A_p).

Applicability of compressive sensing when $M > \frac{N}{2}$: In the cases where the number of measurements M is greater than $\frac{N}{2}$, a natural question arises regarding whether or not there are more equations than the number of variables, and subsequently the applicability of the idea of compressive sensing. However, when we construct a "composite" system matrix such that $\tilde{A} = \begin{pmatrix} A_p \\ A_s \end{pmatrix}$ for various values of M and study its singular value spectrum, the following observations emerge:

(i) Even by the conservative definition of rank, which includes very small but non-zero singular values, the rank of the composite system does not exceed N.

(ii) If we take a more realistic scenario and consider singular values within a factor of 10^6 of the maximum singular value, the number of significant singular values is well below N.

Therefore, even though the composite matrix $\tilde{A}$ is overdetermined, it does not have full column rank. Thus, the use of a priori information towards compressive sensing solutions remains legitimate.

Predictions based on random measurements: The reconstructed tangential fields on the wall are plotted along with the true tangential fields in Fig. 4. It can be seen that the tangential fields are recovered well.

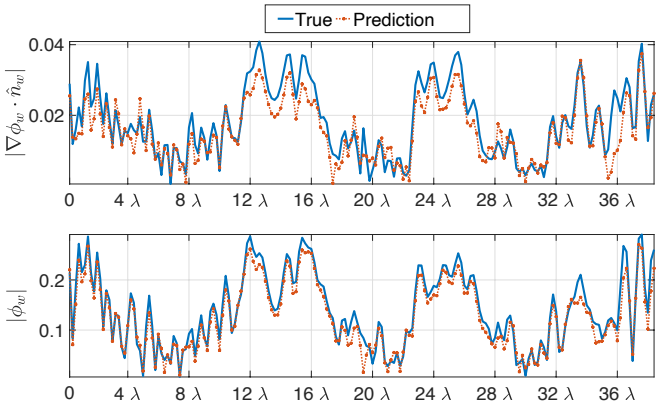

Fig. 4. Comparison of the magnitudes of the estimated and true tangential fields on the surface of the inexact wall, obtained for 387 measurements (0.55 times the number of unknowns). The measurements are noise corrupted by 25 dB SNR.

To visualize field prediction, we consider a contour of ra-

dius 4.2λ centered at origin, which includes all objects and plot the true and predicted fields over it using the CS-SOM method and report the results in Fig. 5. As can be seen, the prediction matches the true field very well. Next, to consider a larger area for prediction, we consider the entire scattering region outside the objects, plotting the true and reconstructed fields in Fig. 6, which again reveal a very good correspondence. Finally, Table 1 shows the tangential field error and the error in reconstruction for various measurement modalities (different number of measurements and SNR values). We also report along with the number of measurements, the *sampling rate* (SR) which is defined as the ratio of the number of measurements to the number of unknowns in the problem. We use the DCT bases and apply the subspace optimization method (see Eq. (10)) for estimating the tangential fields.

In order to study how well our results generalize to different scattering geometries, we also perform experiments with different numbers of objects (one to four). Table 2 shows the tangential field error and the error in reconstruction with different number of objects with a fixed sampling rate of 0.55. As can be seen, the predictions are quite accurate, giving an error of 12% for a sampling rate of 0.55 and 25 dB SNR with a simulation time of 5 minutes per instance of random measurement points. The relative error at each location is shown in Fig. 8, and it can be seen that though the error observed is 12% for 0.55x sampling rate, the major error occurs near the boundary of the walls, and in between close objects. As evidenced by the histogram of error values reported in Fig. 8(b), the prediction accuracy is very good at all the other regions and is less than 10% for more than 80% of the grid locations.

A note on related numerical schemes: It is worth mentioning in passing, the accuracy of three related schemes in solving the above problem.

(i) It is natural to consider a truncated SVD (of the composite matrix $\tilde{A}$) when faced with finding the solution to a linear inverse problem with noisy data. Since this approach does not leverage any a priori information about the problem, the error, not surprisingly, is higher. In particular, we obtain $\Delta_G = 19\%$ and $\Delta_T = 30\%$ in the case of a sampling rate of 0.55 and 25 dB SNR when we retain the minimum number of singular terms so as to satisfy $\|A_p \boldsymbol{x} - b\|_2 < \epsilon$.

(ii) The second approach is to use compressive sensing in a straight forward manner by formulating the problem as:

$$\begin{aligned} \underset{\boldsymbol{\xi}}{\text{minimize}} \quad & \|\boldsymbol{\xi}\|_1 \\ \text{subject to} \quad & \|A_p K \boldsymbol{\xi} - \boldsymbol{b}\|_2 \leq \epsilon, \\ & \|A_s K \boldsymbol{\xi} - \boldsymbol{b}_s\|_2 \leq \eta \end{aligned} \tag{14}$$

where sparsity of the solution in a domain represented by a linear transformation K with coefficients $\boldsymbol{\xi}$ is leveraged for obtaining a solution. Since exact knowledge of the sparsifying domain is not known in general, this approach also leads to a higher error. In our experiments we considered the DFT, DCT, and Wavelet (db-2) transformations, achieving an average of $\Delta_G = 14\%$ and $\Delta_T = 25\%$ in the case of a sampling rate of 0.55 and 25 dB SNR. Our proposed CS-SOM approach gives superior results, and can be thought of as a synthesis of these two 'naive' approaches.

(iii) The third approach is to enforce sparsity by choosing the lower frequency DFT coefficients as the unknowns. We compare CS-SOM to two such reconstruction algorithms, namely the New FFT (NFFT) SOM [21] and the FFT - Twofold SOM (T-SOM) [22]. We find that for a sampling rate of 0.55 and 25 dB SNR, both NFFT SOM and T-SOM achieve an average of $\Delta_G = 15\%$ and $\Delta_T = 30\%$. We do note, however, that CS-SOM has a higher computational run time than NFFT SOM or T-SOM.

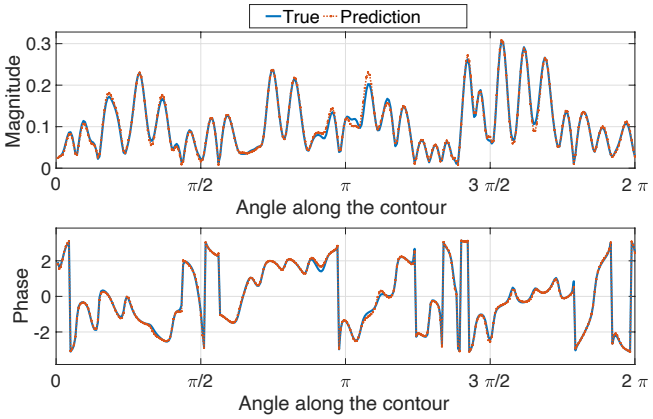

Fig. 5. Comparison of reconstructed and true fields (magnitudes and phase) over a contour of radius 4.2 λ obtained for 0.55x sampling rate (387 measurements). The measurements are noise corrupted by 25 dB SNR.

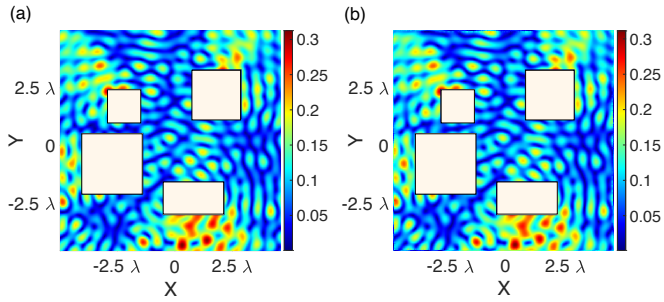

Fig. 6. The magnitude of (a) true and (b) reconstructed 2D fields over a $10\lambda \times 10\lambda$ grid, obtained for 0.55x sampling rate (387 measurements). The measurements are noise corrupted by 25 dB SNR. The colorbar shows the field magnitude in V/m.

5. DISCUSSION

Sparsity in electromagnetic reconstruction problems: In this paper, we have proposed a method of field reconstruction using electromagnetic (EM) principles (Huygens' principle, Extinction theorem) and tangential field sparsity in certain transformed domains. A natural question arises regarding the applicability of sparse reconstruction in general EM problems. This issue has been addressed in [Fig. 6.14 22]. As it turns out, the right singular vectors corresponding to the highest singular values of the state operator resemble low-frequency Fourier bases, whereas those corresponding to the lower singular values resemble high-frequency Fourier bases. If we consider the simple idea of the pseudoinverse of the operator, it becomes clear that the solution is dominated by the highest singular values, and therefore the low-frequency bases. Hence, the idea of imposing sparsity is a general principle in all electromagnetic problems involving radiation-like operators.

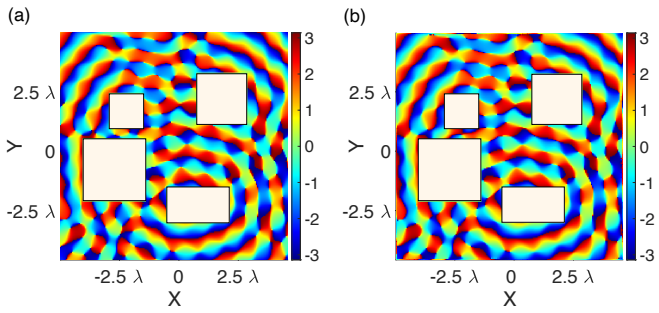

Fig. 7. The phase of (a) true and (b) reconstructed 2D fields over a $10\lambda \times 10\lambda$ grid, obtained for 0.55x sampling rate (387 measurements). The measurements are noise corrupted by 25 dB SNR. The colorbar shows the phase in radians.

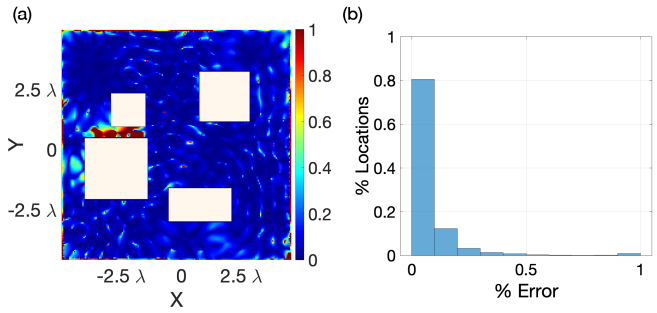

Fig. 8. (a) Relative error (see Eq. (13)) in the prediction of total field over a $10\lambda \times 10\lambda$ grid discretized at $\lambda/20$. The prediction is obtained for 0.55x sampling rate (387 measurements) . The measurements are noise corrupted by 25 dB SNR, and (b) Histogram of normalized error over different locations of the simulation domain in Fig. 8 (a). 80 % of the locations, have less than 10 % prediction error with an average error of 12 %

SNR (dB)		Measurements/Sampling Rate					
		212/ 0.3x		387/0.55x		563/0.8x	
		Δ_G	Δ_T	Δ_G	Δ_T	Δ_G	Δ_T
25	Mean	23	32	12	22	8	19
	Max	32	43	17	29	11	24
	Min	15	24	7	17	5	16
	SD	3	3	2	3	1	2
10	Mean	45	45	31	36	24	30
	Max	54	53	37	41	28	39
	Min	39	39	25	30	20	24
	SD	3	3	2	3	2	3

Table 1. Percentage error in the predicted field (Δ_G) and recovered tangential field (Δ_T) for different measurement modalities (different number of measurements and SNR values) over a $10\lambda \times 10\lambda$ grid calculated for 100 monte carlo trials. SD is the standard deviation.

SNR (dB)		Number of Objects					
		2		3		4	
		Δ_G	Δ_T	Δ_G	Δ_T	Δ_G	Δ_T
25	Mean	10	17	9	17	12	22
	Max	19	13	14	22	17	29
	Min	6	25	6	14	7	11
	SD	3	3	2	2	2	3
10	Mean	30	31	30	32	31	36
	Max	37	38	39	46	37	47
	Min	24	25	27	28	25	30
	SD	3	3	2	4	2	3

Table 2. Percentage error in the predicted field (Δ_G) and recovered tangential field (Δ_T) for different number of objects over a $10\lambda \times 10\lambda$ grid, for 0.55x sampling rate. The error was calculated for 100 monte carlo trials. SD is the standard deviation. The number objects are considered in serial wise as shown in Fig 3.

Extensions of this work: An interesting line of research opens up when we consider the optimality of the sampling locations. To understand this point better, we conducted numerical experiments in which we made field measurements only along an arbitrary line, and found the field prediction to be erroneous. Motivated by this observation, we plan to extend our work by investigating optimal sensor placement and optimal sensing basis with an aim to minimize the number of measurements. There has been promising recent work, both theoretical and computational, in this regard [23–28], though in different settings than those considered here.

Currently, we characterize the error using the sampling rate which is defined as the ratio between the number of measurements and the number of unknowns. The latter is not a fundamental choice and other characterizations, such as the electrical length of the scatterers or the degrees of freedom of the scattered fields [29, 30] are also possible.

An important line of research is to consider the case of phaseless (amplitude-only) measurements. Such an extension would be useful in situations where it is inconvenient/expensive to make measurements with phase. This problem is called 'Phase Retrieval' and has been studied extensively in the literature [31–34]. Traditional approaches like alternating projections [35, 36] often reach a local minima, but more recent advances in this area are based on dictionary learning [37, 38] and have achieved considerable success, even for the case where the number of measurements is smaller than the number of unknowns. Finally, we plan to extend our work to 3 dimensional (3D) scenarios.

Limitations of the proposed method: The method proposed in this paper suffers from the following limitations:
(i) The highest error in prediction occurs at the corners of the outer wall and the regions in-between the objects where very few field measurements are taken. To mitigate the error in between the objects more measurements should be considered in such regions.
(ii) In complex scattering environments with a large number of scatterers, the number of unknowns increases. Since the error

in reconstruction depends on the sampling rate, the number of measurements needed to attain the same level of accuracy is also higher. Further studies on the degrees of freedom inherent in a scattering environment need to be undertaken in order to determine how the number of unknowns scale with the number of scatterers [29, 30, 39].

Summary: In this work, we have shown that when spatial measurements of fields are taken in an indoor scenario, we can recover the electromagnetic fields to varying degrees of accuracy depending on the number and location of measurements. We use the compressive sensing subspace optimization technique to find tangential fields on the surfaces of the scatterers. For example, in the numerical study we undertook within a $10\lambda \times 10\lambda$ region, the electromagnetic fields can be recovered with 387 measurements upto an error of $\approx 12\%$.

Future applications: The method described in this paper can be employed in a number of scenarios, a few of which are mentioned here. Since our method correctly reconstructs the tangential fields on a contour bounding the object, a logical extension is the prediction of the radar cross-section (RCS) of the scattering object using a near-to-far field transformation (see [1] for example). RCS estimation is known to be a time intensive process, and any improvement that can be attained by minimizing the number of measurements required is welcome. Next, indoor Positioning Systems can employ this method, instead of ray tracing methods (e.g. [40–42]) to determine the location of a person based on EM field measurements. To counter uniqueness problems (where two or more locations have approximately the same field magnitude), multiple frequency sources can be employed, and or data can be collected from several locations. Finally, our method can also be applied to WiFi access point planning, in which one tries to optimally place WiFi routers in an environment so that most locations receive good Quality of Service (QoS) guarantees.

ACKNOWLEDGEMENTS

We are very grateful to the anonymous reviewers for providing valuable feedback that has led to a significant improvement in the quality of our manuscript.

REFERENCES

1. T. B. Hansen, R. A. Marr, U. H. Lammers, T. J. Tanigawa, and R. V. McGahan, "Bistatic rcs calculations from cylindrical near-field measurements—part i: Theory," IEEE transactions on antennas propagation **54**, 3846–3856 (2006).
2. L. Pei, R. Chen, J. Liu, H. Kuusniemi, T. Tenhunen, and Y. Chen, "Using inquiry-based bluetooth rssi probability distributions for indoor positioning," J. Glob. Position. Syst. **9**, 122–130 (2010).
3. Z.-H. Wu, Y. Han, Y. Chen, and K. R. Liu, "A time-reversal paradigm for indoor positioning system," IEEE Transactions on Veh. Technol. **64**, 1331–1339 (2015).
4. A. Bose and C. H. Foh, "A practical path loss model for indoor wifi positioning enhancement," in *Information, Communications & Signal Processing, 2007 6th International Conference on,* (IEEE, 2007), pp. 1–5.
5. A. Toscano, F. Bilotti, and L. Vegni, "Fast ray-tracing technique for electromagnetic field prediction in mobile communications," IEEE transactions on magnetics **39**, 1238–1241 (2003).
6. V. Degli-Esposti, D. Guiducci, A. de'Marsi, P. Azzi, and F. Fuschini, "An advanced field prediction model including diffuse scattering," IEEE Transactions on Antennas Propag. **52**, 1717–1728 (2004).
7. Z. Ji, B.-H. Li, H.-X. Wang, H.-Y. Chen, and T. K. Sarkar, "Efficient ray-tracing methods for propagation prediction for indoor wireless communications," IEEE Antennas Propag. Mag. **43**, 41–49 (2001).
8. K. A. Remley, H. R. Anderson, and A. Weisshar, "Improving the accuracy of ray-tracing techniques for indoor propagation modeling," IEEE transactions on vehicular technology **49**, 2350–2358 (2000).
9. W. C. Chew, *Waves and fields in inhomogeneous media* (IEEE press, 1995).
10. S. Boyd and L. Vandenberghe, *Convex optimization* (Cambridge university press, 2004).
11. A. Massa, P. Rocca, and G. Oliveri, "Compressive sensing in electromagnetics-a review," IEEE Antennas Propag. Mag. **57**, 224–238 (2015).
12. G. Oliveri, M. Salucci, N. Anselmi, and A. Massa, "Compressive sensing as applied to inverse problems for imaging: Theory, applications, current trends, and open challenges." IEEE Antennas Propag. Mag. **59**, 34–46 (2017).
13. F. Viani, L. Poli, G. Oliveri, F. Robol, and A. Massa, "Sparse scatterers imaging through approximated multitask compressive sensing strategies," Microw. Opt. Technol. Lett. **55**, 1553–1558 (2013).
14. M. Bevacqua, L. Crocco, L. Di Donato, and T. Isernia, "Microwave imaging of nonweak targets via compressive sensing and virtual experiments," IEEE Antennas Wirel. Propag. Lett. **14**, 1035–1038 (2014).
15. X. Chen, "Subspace-based optimization method for solving inverse-scattering problems," IEEE Transactions on Geosci. Remote. Sens. **48**, 42–49 (2009).
16. Y. Sanghvi, Y. N. G. B. Kalepu, and U. Khankhoje, "Embedding deep learning in inverse scattering problems," IEEE Transactions on Comput. Imaging (2019).
17. C. A. Balanis, *Advanced engineering electromagnetics* (John Wiley & Sons, 1999).
18. D. K. Sastry, C. Bhat, and U. K. Khankhoje, "Spatial prediction of undersampled electromagnetic fields," in *2019 PhotonIcs & Electromagnetics Research Symposium-Spring (PIERS-Spring),* (IEEE, 2019), pp. 131–138.
19. V. Morozov and A. Grebennikov, *Methods for solution of Ill-posed problems: algorithmic aspects* (Moscow univ. press Moscow, 2005).
20. E. J. Candès and M. B. Wakin, "An introduction to compressive sampling [a sensing/sampling paradigm that goes against the common knowledge in data acquisition]," IEEE signal processing magazine **25**, 21–30 (2008).
21. Z. Wei, R. Chen, H. Zhao, and X. Chen, "Two fft subspace-based optimization methods for electrical impedance tomography," Prog. In Electromagn. Res. **157**, 111–120 (2016).
22. X. Chen, *Computational methods for electromagnetic inverse scattering* (Wiley Online Library, 2018).
23. S. Joshi and S. Boyd, "Sensor selection via convex optimization," IEEE Transactions on Signal Process. **57**, 451–462 (2008).
24. J. Ranieri, A. Chebira, and M. Vetterli, "Near-optimal sensor placement for linear inverse problems," IEEE Transactions on signal processing **62**, 1135–1146 (2014).
25. C. Jiang, Y. C. Soh, and H. Li, "Sensor placement by maximal projection on minimum eigenspace for linear inverse problems," IEEE Transactions on Signal Process. **64**, 5595–5610 (2016).
26. S. Liu, S. P. Chepuri, M. Fardad, E. Maşazade, G. Leus, and P. K. Varshney, "Sensor selection for estimation with correlated measurement noise," IEEE Transactions on Signal Process. **64**, 3509–3522 (2016).
27. R. Obermeier and J. A. Martinez-Lorenzo, "Sensing matrix design via mutual coherence minimization for electromagnetic compressive imaging applications," IEEE Transactions on Comput. Imaging **3**, 217–229 (2017).
28. R. Solimene, M. A. Maisto, and R. Pierri, "Sampling approach for singular system computation of a radiation operator," JOSA A **36**, 353–361 (2019).
29. O. M. Bucci and G. Franceschetti, "On the degrees of freedom of scattered fields," IEEE transactions on Antennas Propag. **37**, 918–926 (1989).

30. R. Piestun and D. A. Miller, "Electromagnetic degrees of freedom of an optical system," JOSA A **17**, 892–902 (2000).
31. P. Netrapalli, P. Jain, and S. Sanghavi, "Phase retrieval using alternating minimization," in *Advances in Neural Information Processing Systems 26,* C. J. C. Burges, L. Bottou, M. Welling, Z. Ghahramani, and K. Q. Weinberger, eds. (Curran Associates, Inc., 2013), pp. 2796–2804.
32. E. J. Candes, Y. C. Eldar, T. Strohmer, and V. Voroninski, "Phase retrieval via matrix completion," SIAM review **57**, 225–251 (2015).
33. K. Jaganathan, Y. C. Eldar, and B. Hassibi, "Phase retrieval: An overview of recent developments," arXiv preprint arXiv:1510.07713 (2015).
34. J. Sun, Q. Qu, and J. Wright, "A geometric analysis of phase retrieval," Foundations Comput. Math. **18**, 1131–1198 (2018).
35. R. Gerchberg and W. Saxton, "A practical algorithm for the determination of the phase from image and diffraction plane pictures," Optik. **35**, 237 (1972).
36. J. R. Fienup, "Phase retrieval algorithms: a comparison," Appl. optics **21**, 2758–2769 (1982).
37. A. M. Tillmann, Y. C. Eldar, and J. Mairal, "Dolphin—dictionary learning for phase retrieval," IEEE Transactions on Signal Process. **64**, 6485–6500 (2016).
38. T. Qiu and D. P. Palomar, "Undersampled sparse phase retrieval via majorization–minimization," IEEE Transactions on Signal Process. **65**, 5957–5969 (2017).
39. J. Xu and R. Janaswamy, "Electromagnetic degrees of freedom in 2-d scattering environments," IEEE transactions on antennas propagation **54**, 3882–3894 (2006).
40. A. Tayebi, J. Gomez Perez, F. M. S. d. Adana Herrero, and O. Gutierrez Blanco, "The application of ray-tracing to mobile localization using the direction of arrival and received signal strength in multipath indoor environments," Prog. In Electromagn. Res. **91**, 1–15 (2009).
41. C. Sturm, W. Sorgel, T. Kayser, and W. Wiesbeck, "Deterministic uwb wave propagation modeling for localization applications based on 3d ray tracing," in *2006 IEEE MTT-S International Microwave Symposium Digest,* (IEEE, 2006), pp. 2003–2006.
42. O. Katircioglu, H. Isel, O. Ceylan, F. Taraktas, and H. B. Yagci, "Comparing ray tracing, free space path loss and logarithmic distance path loss models in success of indoor localization with rssi," in *2011 19thT-elecommunications Forum (TELFOR) Proceedings of Papers,* (IEEE, 2011), pp. 313–316.